aerospace

MDPI

Article

Detached Eddy Simulations of Cavity-Store Interactions at Subsonic Turbulent Flow

Hadar Ben-Gida

Aeronautical Engineering Branch, Israeli Air Force, Tel Aviv 6473428, Israel; bengida@idf.il

Abstract: Weapons bays have gained much attraction in the last decade, mainly in the context of next-generation aircraft. Although internal store carriage provides numerous advantages, aero-mechanical challenges still exist, particularly for safe store separation. Therefore, it is essential to gain fundamental knowledge of the flow field within weapons bays, which can be achieved by studying the flow within a more simplified geometry of a cavity. In this study, detached eddy simulations are performed using the Elastic-Zonal-Navier–Stokes-Solver (EZNSS) to characterize the unsteady turbulent flow within NASA's benchmark rectangular cavity with a store model located at various positions. Simulations are performed at a Mach number of 0.4 and a Reynolds number of 7 million to form a transitional cavity flow, which is common in jet-fighter weapons bays. The numerical results are validated with experimental data for the empty cavity and cavity-with-store configurations. The effect of the store's position on the cavity flow characteristics is analyzed and verified, as well as the aerodynamic loads exerted on the store. Results show a complex interaction between the store model and the cavity flow field, manifested by distortion of the wall pressure fluctuations and mean flow structures and large amplitude fluctuations of the loads exerted on the store. The insights reported herein can serve future development efforts of more accurate numerical frameworks for cavity-with-store configurations towards improving their applicability for weapons bays store separation in certification procedures.

Keywords: cavity; CFD; DES; store separation

Citation: Ben-Gida, H. Detached Eddy Simulations of Cavity-Store Interactions at Subsonic Turbulent Flow. *Aerospace* **2023**, *10*, 935. https://doi.org/10.3390/aerospace10110935

Academic Editor: Lawrence S. Ukeiley

Received: 28 September 2023
Revised: 28 October 2023
Accepted: 30 October 2023
Published: 31 October 2023

1. Introduction

The use of internal weapons bays in modern military aircraft is on the rise, offering distinct advantages over conventional external store carriage, such as drag reduction and minimized radar cross-section. However, internal store carriage still has aero-mechanical challenges, particularly when opening the weapons bay doors and releasing stores. In such scenarios, the bay is exposed to the free-stream air, which induces the formation of a highly turbulent and unsteady flow field, known as 'cavity flow'. This turbulent flow can lead to pressure fluctuations within the bay, which potentially induce acoustical tones that can endanger nearby electronics and alter the trajectories of released stores [1,2], due to the large variation of the forces and moments exerted on them [3–6]. These dynamic variations in the store loads during separation phases can result in hazardous collisions between stores and the aircraft, emphasizing the importance of understanding the fundamental flow characteristics within weapons bays for advanced next-generation aircraft design.

Although studying realistic weapons bays is appealing, a common alternative to gain insight into the fundamental flow physics within is by studying cavity geometries [7]. Cavity flow is considered as the flow, with velocity U_∞, parallel to a rectangular cutout (cavity) in a flat plate (see Figure 1). The cavity dimensions are given by L (length), H (height or depth), and W (width). Here, the cavity is characterized by a right-handed Cartesian coordinate system (x, y, z), originating at the centerline of the cavity front (upstream) wall leading-edge. The corresponding velocity components of the flow are denoted by (u, v, w). Typically, flow within a cavity exhibits a highly three-dimensional and unsteady nature due

to the breakdown of the shear layer at the front wall, which induces the Kelvin–Helmholtz instability [7]. As the shear layer vortices interact with the cavity's aft wall, pressure perturbations generate acoustic waves that propagate outwards and back to the front wall. Consequently, the full three-dimensional characterization of cavity flow can be challenging. Nevertheless, it is common in the literature to characterize the cavity flow based on its time-averaged two-dimensional patterns, as proposed by Charwat et al. [8]. Based on the time-averaged flow patterns observed in experimental studies, three principal flow types are identified: 'open', 'closed', and 'transitional' [8–10], where the primary parameter to distinguish between these flow types is the cavity length-to-height ratio (L/H).

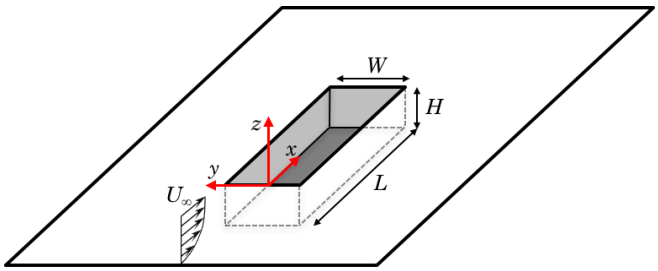

Figure 1. Schematics of flow parallel to a rectangular cutout (cavity) in a flat plate.

According to Plentovich et al. [11], open cavity flows, often referred to as 'deep' cavities, manifest when the length-to-height ratio (L/H) falls below 6–8. Under such conditions, the shear layer detaches from the cavity's front wall and reattaches either on or downstream of the cavity's aft wall. This phenomenon leads to the formation of a large re-circulation zone within the cavity with the time-averaged static pressure at the cavity floor being mostly constant [11], which can be favorable for store separation. However, these conditions result in the generation of strong periodic pressure fluctuations, which induce high-amplitude narrow-band tones that can damage nearby electronic systems [12]. In contrast, closed cavity flows ('shallow' cavities) correspond to length-to-height ratios of $L/H > 10 - 15$ [11]. In these configurations, the separated shear layer from the front wall of the cavity impinges the cavity floor, leading to a region of high static pressure in the aft section of the cavity floor. The significant pressure variation along the cavity floor can adversely affect the store separation process, potentially inducing significant pitch-up moments on the store [4]. Transitional cavity flows, representing an intermediate category between open and closed cases, are characterized by a separated shear layer that flows into and out of the cavity without impinging the cavity floor. As a result, cavities exhibiting transitional flow may pose challenges for both safe store separation and controlling the acoustic disturbances within the cavity [12]. Interestingly, it appears that many fifth-generation jet-fighters, including the Chengdu J-20, Sukhoi Su-57, Lockheed Martin F-22 Raptor, and F-35 Lightning II, employ weapons bay geometries that are expected to operate in the transitional flow regime. Therefore, gaining an in-depth understanding of the fundamental physics governing transitional cavity flow can significantly improve future designs of weapons bays in jet-fighters.

Over the years, extensive research efforts have been dedicated to study the characteristics of cavity flows within the context of weapon bays [7]. However, the substantial costs associated with wind tunnel tests and the relatively limited success of theoretical models have led to a growing focus in utilizing computational approaches for analyzing cavity flows over the last decade. Among the computational methods available, unsteady Reynolds-averaged Navier–Stokes (URANS) stands out as a relatively cost-effective means of simulating unsteady turbulent flows within cavities. URANS simulations published in the literature have demonstrated good agreement with experimental data in terms of the mean pressure distribution along the cavity floor. However, discrepancies have been reported on the cavity's aft wall, where the largest fluctuating pressure values are [7]. Moreover, although URANS methods were found to accurately predict the low-frequency

acoustic tones in the cavity (associated with the large turbulent scales), no success has been reported in resolving the high-frequency tones (small scales) and the broadband noise [13]. Given the substantial levels of turbulent viscosity generated by URANS approaches, they are currently considered inadequate for accurately modeling the turbulent flow structures within cavities [14]. Consequently, researchers have embarked on exploring more advanced computational techniques, such as large-eddy simulation (LES) approaches. In LES modeling, the Navier–Stokes equations are filtered, allowing for the computation of large turbulent scales, whereas smaller scales are modeled using a sub-grid scale model [15]. Although LES has demonstrated a good agreement with experimental results, it demands significant computational resources to effectively resolve high-Reynolds cavity flows because the near-wall grid resolution approaches direct numerical simulation (DNS) standards [7].

It becomes evident that both URANS and LES encounter limitations when simulating cavity flows at high-Reynolds numbers. URANS, although computationally efficient, lacks the necessary accuracy for resolving the relevant turbulent scales in a cavity. Conversely, LES offers higher fidelity but at a significant computational cost that remains impractical for many real-world applications. Therefore, many studies adopted a hybrid RANS/LES approach, which integrates the advantages of both RANS and LES methods, known as detached eddy simulation (DES). The hybrid model uses the RANS method for solving the near-wall flow field regions and switches to LES further away from the wall. This dual-mode strategy effectively addresses the demand for high grid resolution near the wall, a prerequisite for accurate LES simulations. It should be noted that generating a grid for DES must be done carefully, as most hybrid models depend on the grid resolution to activate the switch between RANS and LES modes. In the context of cavity flow simulations, hybrid RANS/LES methods have exhibited superior performance compared to RANS, closely aligning with experimental data, with lower computational costs than LES [7,13,16–25]. Therefore, in this study, we used the hybrid RANS/LES method to resolve the cavity flow, as described in the numerical approach section.

The first hybrid model, developed by Spalart et al. [26], is based on the Spalart–Allmaras (S–A) one-equation turbulence model [27] and is referred to as S–A DES. This model relies on wall distance as its length scale, employed to increase the destruction term in shear layers and regions distant from walls. This adjustment effectively diminishes the turbulent viscosity (μ_t) to levels consistent with the LES sub-grid model. The hybrid model operates in a RANS mode when grid points reside in the near-wall region. Otherwise, the model becomes grid-dependent and performs as a sub-grid scale version of the baseline S–A model in regions distanced from walls. The dependency in the wall distance was later resolved by introducing 'topology-free' models. For example, the extra-large-eddy simulation (X-LES) model developed by Kok et al. [28] and based on the k-ω turbulent/non-turbulent (TNT) turbulence model [29] eliminates the need for explicit wall distance. Rokita [20] has successfully implemented the X-LES model in resolving the subsonic flow field inside a rectangular cavity, reporting good agreement with experimental data.

Among the first to study stores within cavities were Rossiter and Kurn [30]. Through wind tunnel measurements, they found that introducing a store into a cavity results in a reduction of the pressure fluctuations. Building upon Rossiter and Kurn's study, Stallings et al. [4] performed wind tunnel tests to investigate how the cavity geometry affects the aerodynamic forces and moments exerted on a generic store model. Results showed that the normal/lateral positioning of the store had minimal effect on the cavity flow type, with only slight variations in the cavity pressure fluctuations and the store forces and moments. Increasing the Mach number showed a subtle effect on the store forces and moments for closed cavity flows while significantly reducing the pitching moment for transitional cavity flows. Despite the accumulation of a substantial volume of experimental data over the years, conducting wind tunnel experiments of cavities with stores remains a formidable challenge [31,32]. Even non-intrusive techniques, such as particle image velocimetry (PIV) and pressure-sensitive paint (PSP), which offer high spatial and temporal

resolutions [33–35], encounter limitations in applications involving relatively complex cavity geometries at high-Reynolds and high-Mach flows due to their intricate setups. Consequently, a significant portion of the research efforts in recent years has focused on resolving the full three-dimensional and unsteady flow field within the cavities and around stores with hybrid RANS/LES methods.

Roughen et al. [36] were among the first to utilize the S–A DES model for simulating the transitional flow in a cavity ($L/H = 7$) with an MK-82 JDAM store at $M_\infty = 0.8$. The simulation data enabled them to predict store trajectories for the separation phase, which agreed well with experimental data. In addition, Kim et al. [21] studied the transonic flow field ($M_\infty = 0.95$) in a deep weapons bay ($L/H = 4.5$) with a store using a k-ω SST DES model. Their work unveiled the substantial impact of pressure fluctuations on store trajectory, particularly during the initial stages of separation. Moreover, Barone and Arunajatesan [37] studied the development of acoustic tones within a deep cavity ($L/H = 3.33$) with a store model at $M_\infty = 0.6 - 1.47$ using the k-ϵ DES method. Their findings highlighted a complex relationship between the cavity acoustic tones and the resulting forces on the store. Furthermore, Babu et al. [23] have employed the S–A DES model in conjunction with a tightly coupled aeroelastic method to study the effect of flexible fins on the aerodynamic loads acting on a store placed at different locations within a rectangular cavity of $L/H = 7$ and $W/H = 2$. Results at $M_\infty = 0.85$ have shown that the fluid-structure interaction strongly affects the cavity's frequency content, whereas the store loads are only slightly affected. Yan et al. [38] have recently studied the trajectory of a generic store ejected at supersonic conditions from the M219 cavity ($L/H = 5$) by utilizing the improved delayed detach-eddy simulation (IDDES) model that is based on the k-ω SST turbulence model. Their results have demonstrated the strong interplay between the spectral content in the cavity and the store location during the separation process.

With the growing prevalence of internal weapon bays in aircraft, there is an increasing demand for accurate computational predictions of store separation from weapons bays. Although the use of hybrid RANS/LES models in simulating the flow within cavities with stores has grown in the last decade, only a few studies presented a comparison with experimental data, thus emphasizing the need for extensive numerical validation. In the present study, we utilized a hybrid RANS/LES modeling approach to resolve the unsteady flow within NASA's benchmark case of a rectangular cavity with a generic store [4]. Our focus centers on investigating the transitional cavity flow type [11], a regime that is highly relevant to fifth-generation jet-fighters. We therefore studied NASA's cavity model with dimensions of $L/H = 6.25$ and $W/H = 2$, at sea-level altitude (standard atmosphere), free-stream Mach number of $M_\infty = 0.40$, and Reynolds number of $Re_L = \rho U_\infty L/\mu = 7 \times 10^6$, where ρ and μ are the density and dynamic viscosity of air. The numerical results are validated with the experimental data for both an empty cavity configuration and a cavity configuration with a store model placed at various locations within (cavity-with-store configurations) [4]. The effect of the store location on the cavity flow characteristics is computed and analyzed, as well as the forces and moments exerted on the store. The insights gained in this study can be valuable in simulating cavity-with-store configurations, potentially improving future computational efforts of store separation from internal bays.

2. Numerical Approach

2.1. Flow Solver

Numerical flow simulations were conducted using the EZNSS CFD code [39], developed by the Israeli CFD center (ISCFDC). It is a chimera-based Navier–Stokes flow solver for simulating time-accurate flows about dynamically deforming geometries. The chimera grid scheme [40] enables simulating moving bodies as well as modeling complex geometries. The code is based on finite differences schemes and utilizes the formulation of the Navier–Stokes equations in curvilinear coordinates; second-order accuracy is available in both the spatial and temporal domains. Various algorithms are implemented for the

convective fluxes, as well as several turbulence models and a dual time-step procedure. The code is fully parallel, using multi-level parallelization for the flow solver [41].

2.2. Turbulence Model

In this study, the flow within the cavity is modeled using the X-LES model developed by Kok et al. [28], which is based on the two-equation k-ω TNT turbulence model. As mentioned above, the X-LES TNT model offers a topology-free approach, which is highly beneficial for RANS/LES simulations. Moreover, unlike other two-equation turbulence models, the TNT turbulence mode reduces the sensitivity to the specific turbulence dissipation rate free-stream boundary condition. The X-LES TNT model comprises a composite formulation incorporating RANS and LES equations. A defined sub-grid-scale (SGS) model is used for the LES mode, in which the two-equation turbulence model degenerates into one equation of the turbulence kinetic energy of the SGS model.

The hybrid turbulence model can be written in a general, unified formulation as [39]:

$$\frac{\partial \mathbf{q}}{\partial \tau} + \frac{\partial \mathbf{f}}{\partial \xi} + \frac{\partial \mathbf{g}}{\partial \eta} + \frac{\partial \mathbf{h}}{\partial \zeta} = \frac{\partial \mathbf{f}_v}{\partial \xi} + \frac{\partial \mathbf{g}_v}{\partial \eta} + \frac{\partial \mathbf{h}_v}{\partial \zeta} + \frac{\boldsymbol{S}}{J}, \tag{1}$$

where $\mathbf{q} = [\rho k, \rho\omega]^T / J$ is the solution vector, and k and ω correspond to the turbulence kinetic energy and specific turbulence dissipation rate, respectively. J is the Jacobian of the transformation matrix relating the physical domain (t, x, y, z) to the computational one (τ, ξ, η, ζ). The terms $\mathbf{f}$, $\mathbf{g}$, and $\mathbf{h}$ represent the inviscid rotated fluxes:

$$\begin{aligned} \mathbf{f} &= \frac{1}{J}[\rho k U, \rho\omega U]^T \\ \mathbf{g} &= \frac{1}{J}[\rho k V, \rho\omega V]^T \\ \mathbf{h} &= \frac{1}{J}[\rho k W, \rho\omega W]^T, \end{aligned} \tag{2}$$

where U, V, and W are the contravariant velocities, expressed as:

$$\begin{bmatrix} U - \partial\xi/\partial t \\ V - \partial\eta/\partial t \\ W - \partial\zeta/\partial t \end{bmatrix} = \begin{bmatrix} \partial\xi/\partial x & \partial\xi/\partial y & \partial\xi/\partial z \\ \partial\eta/\partial x & \partial\eta/\partial y & \partial\eta/\partial z \\ \partial\zeta/\partial x & \partial\zeta/\partial y & \partial\zeta/\partial z \end{bmatrix} \begin{bmatrix} u \\ v \\ w \end{bmatrix}. \tag{3}$$

Each element containing derivatives with respect to the original independent variables (t, x, y, z) in Equation (3) has to be expanded following the chain rule so that the final form of the equations includes only derivatives with respect to the transformed independent variables (τ, ξ, η, ζ). The terms $\mathbf{f}_v$, $\mathbf{g}_v$, and $\mathbf{h}_v$ represent the rotated viscous fluxes:

$$\mathbf{f}_v = \frac{1}{J}\left[\frac{\partial\left(\mu_k \tilde{\nabla} k \cdot \frac{\partial \Theta}{\partial x}\right)}{\partial \xi}, \frac{\partial\left(\mu_\omega \tilde{\nabla} \omega \cdot \frac{\partial \Theta}{\partial x}\right)}{\partial \xi}\right]^T \tag{4}$$

$$\mathbf{g}_v = \frac{1}{J}\left[\frac{\partial\left(\mu_k \tilde{\nabla} k \cdot \frac{\partial \Theta}{\partial y}\right)}{\partial \eta}, \frac{\partial\left(\mu_\omega \tilde{\nabla} \omega \cdot \frac{\partial \Theta}{\partial y}\right)}{\partial \eta}\right]^T \tag{5}$$

$$\mathbf{h}_v = \frac{1}{J}\left[\frac{\partial\left(\mu_k \tilde{\nabla} k \cdot \frac{\partial \Theta}{\partial z}\right)}{\partial \zeta}, \frac{\partial\left(\mu_\omega \tilde{\nabla} \omega \cdot \frac{\partial \Theta}{\partial z}\right)}{\partial \zeta}\right]^T, \tag{6}$$

with $\boldsymbol{\Theta} = [\xi, \eta, \zeta]$, $\tilde{\nabla} = \left[\frac{\partial}{\partial\xi}, \frac{\partial}{\partial\eta}, \frac{\partial}{\partial\zeta}\right]$, $\mu_k = (\mu + \mu_t/\sigma_k)$, and $\mu_\omega = (\mu + \mu_t/\sigma_\omega)$. The source vector, $\boldsymbol{S}$, is computed accordingly:

$$\boldsymbol{S} = \begin{Bmatrix} P_k - \rho\frac{k^{1.5}}{l_k} \\ \alpha_\omega \frac{\omega}{k} P_k - \beta_\omega \rho\omega^2 + \max(\epsilon, 0) \end{Bmatrix}, \tag{7}$$

where ϵ is the cross-diffusion term given by:

$$\epsilon = \sigma_d \frac{\rho}{\omega}\left[\tilde{\nabla}k \cdot \frac{\partial\boldsymbol{\Theta}}{\partial x}\tilde{\nabla}\omega \cdot \frac{\partial\boldsymbol{\Theta}}{\partial x} + \tilde{\nabla}k \cdot \frac{\partial\boldsymbol{\Theta}}{\partial y}\tilde{\nabla}\omega \cdot \frac{\partial\boldsymbol{\Theta}}{\partial y} + \tilde{\nabla}k \cdot \frac{\partial\boldsymbol{\Theta}}{\partial z}\tilde{\nabla}\omega \cdot \frac{\partial\boldsymbol{\Theta}}{\partial z}\right]. \tag{8}$$

The production term is denoted by P_k, and it is based on the Boussinesq approximation:

$$P_k = \left\{\mu_t\left[\left(\frac{\partial u_i}{\partial x_j} + \frac{\partial u_j}{\partial x_i}\right) - \frac{2}{3}\delta_{ij}\frac{\partial u_k}{\partial x_k}\right] - \frac{2}{3}\rho k\delta_{ij}\right\}\frac{\partial u_i}{\partial x_j}. \tag{9}$$

The turbulent length scale is denoted by l_k, given here by the RANS-LES switch as follows:

$$l_k = \min(l_{\text{RANS}}, l_{\text{LES}}), \tag{10}$$

where the background RANS model length scale, l_{RANS}, is expressed by:

$$l_{\text{RANS}} = \frac{\sqrt{k}}{\beta_k \omega}, \tag{11}$$

and l_{LES} is the LES length scale defined with the sub-grid length scale, Δ:

$$l_{\text{LES}} = C_{\text{DES}}\Delta, \tag{12}$$

with $C_{\text{DES}} = 0.65$. In the present work, the sub-grid length scale, Δ, is calculated according to Abe [42]:

$$\Delta = \sqrt{\frac{\delta_\xi \delta_\eta \delta_\zeta}{\min(\delta_\xi, \delta_\eta, \delta_\zeta)}}, \tag{13}$$

where δ_ξ, δ_η, and δ_ζ are the computational grid spacings of the generalized curvilinear coordinates. Finally, the turbulent viscosity is defined accordingly:

$$\mu_t = \min\left(\frac{\sqrt{k}}{\omega}, C_1\Delta\right)\rho\sqrt{k}. \tag{14}$$

The remaining model constants are $\sigma_k = 1.5$, $\sigma_\omega = 2.0$, $\sigma_d = 0.5$, $\beta_\omega = 0.075$, $\beta_k = 0.09$, $\alpha_\omega = 0.5532$, and $C_1 = 0.06$.

2.3. Computational Domains

Two configurations were investigated in this study: an empty cavity and a cavity with a generic store model (placed at various locations), as detailed below.

2.3.1. Empty Cavity Configuration

The geometries of the cavity and its surrounding plate are based on the wind tunnel model tested by Stallings et al. [4], as depicted in Figure 1. The origin of the coordinate system $\vec{x} = (x, y, z)$ is at the centerline of the cavity front wall leading-edge (see Figure 1), where the x, y, and z axes correspond to the streamwise, spanwise, and normal directions. The cavity dimensions used for the current study are $L = 750$ mm, $H = 120$ mm, and $W = 240$ mm ($L/H = 6.25$ and $W/H = 2$), which correspond to an open-transitional flow type [11]. The front plate upstream section (ahead of the cavity) has a length of 0.9144 m for the turbulent boundary layer to develop and reach the leading-edge of the cavity front wall

with the thickness measured by Stallings et al. [4], $\delta_{EXP} = 12$ mm. The aft plate section has a length of 6.75 m, which is longer than the model used by Stallings et al. [4]. This allows for proper propagation of pressure perturbations and vortical structures shed downstream from the cavity, thus preventing any numerical artifacts of the flow field within the cavity. The width of the plate was 3.6 m.

The three-dimensional cavity mesh topology comprises three overlapping grids utilizing the chimera approach, with a total of 3.9 million nodes within the cavity, as depicted in Figure 2. All overlapping zones allow double fringe interpolation to maintain spatial accuracy. A 'hyperbolic-like' grid topology was chosen for the upper part of the cavity (green-colored 'elliptical-shape' grid depicted in Figure 2d); thus, allowing boundary layer grid clustering just upon walls and not within the shear layer region. The inner part of the cavity is meshed using two grids: one is attached to the cavity walls and overlaps with the 'elliptical-shape' grid (black-colored rectangular grid depicted in Figure 2b,d), and another is 'floating' to cover the remaining inner region of the cavity (purple-colored grid depicted in Figure 2b).

The plate surrounding the cavity is meshed using four rectangular grids. Two grids are attached to the plate wall (yellow- and green-colored grids depicted in Figure 2c), whereas the remaining two are 'floating' far-field grids (cyan- and red-colored grids depicted in Figure 2a). The plate-cavity boundary is meshed using four more grids. These grids account for the fore, aft, and spanwise cavity boundaries with the plate (black-, pink-, and blue-colored grids in Figure 2d).

All normal wall spacings were set to 5 µm to allow good resolution of the boundary layer ($y^+ \sim O(1)$). The average characteristic cell size within the cavity volume is $(\Delta x, \Delta y, \Delta z) = (5, 5, 5)$ mm. In total, the empty cavity configuration included about 11 million nodes.

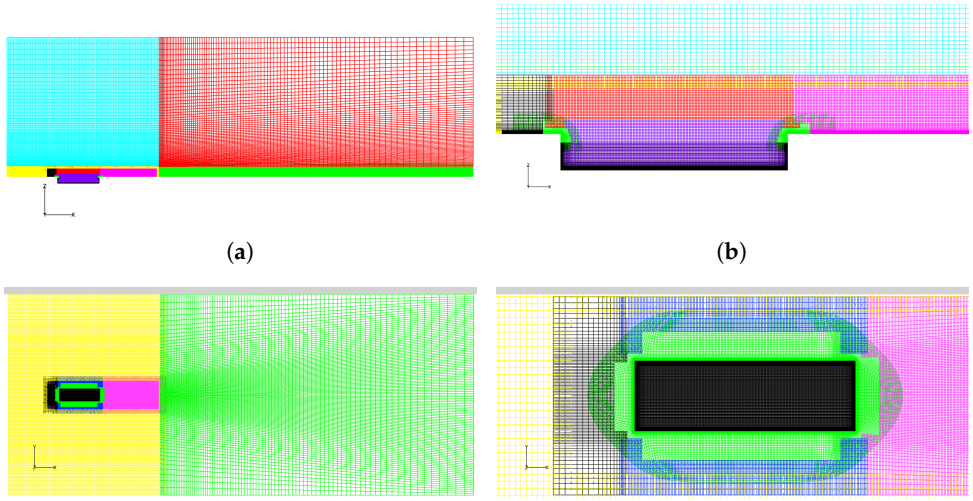

Figure 2. The computational domain of the empty cavity configuration. (**a**) $y = 0$ plane view; (**b**) zoom-in $y = 0$ plane view; (**c**) upper view; (**d**) zoom-in upper view.

2.3.2. Cavity-with-Store Configurations

For these configurations, a generic store model was placed within the cavity domain at various positions (see Figure 2) based on the wind tunnel tests published by Stallings et al. [4]. The store model has a length of $L_s = 612.8$ mm, a maximum diameter of $D = 30.5$ mm, an ogive nose shape, and no canards, wings, or fins [4]. The location of the store within the cavity is evaluated by the position of its nose tip, which is denoted by (x_s, y_s, z_s) in the right-handed Cartesian coordinate system of the cavity. The longitudinal location of the store's nose tip was set at $x_s = 30$ mm for all configurations studied here. Simulations were conducted for a store that is placed at two lateral positions: $y_s = 0$ mm

(cavity centerline), and $y_s = 61\,\text{mm}$ ($y_s/D = 2$). For each lateral position, the store was simulated at six different normal positions, $z_s = [-76.2, -50.8, -25.4, 0, 25.4, 50.8]\,\text{mm}$, or in normalized form $z_s/D = [-2.5, -1.67, -0.83, 0, 0.83, 1.67]$, for which experimental aerodynamic data is available from Stallings et al. [4]. In total, twelve cavity-with-store configurations were investigated here, as depicted in Figure 3.

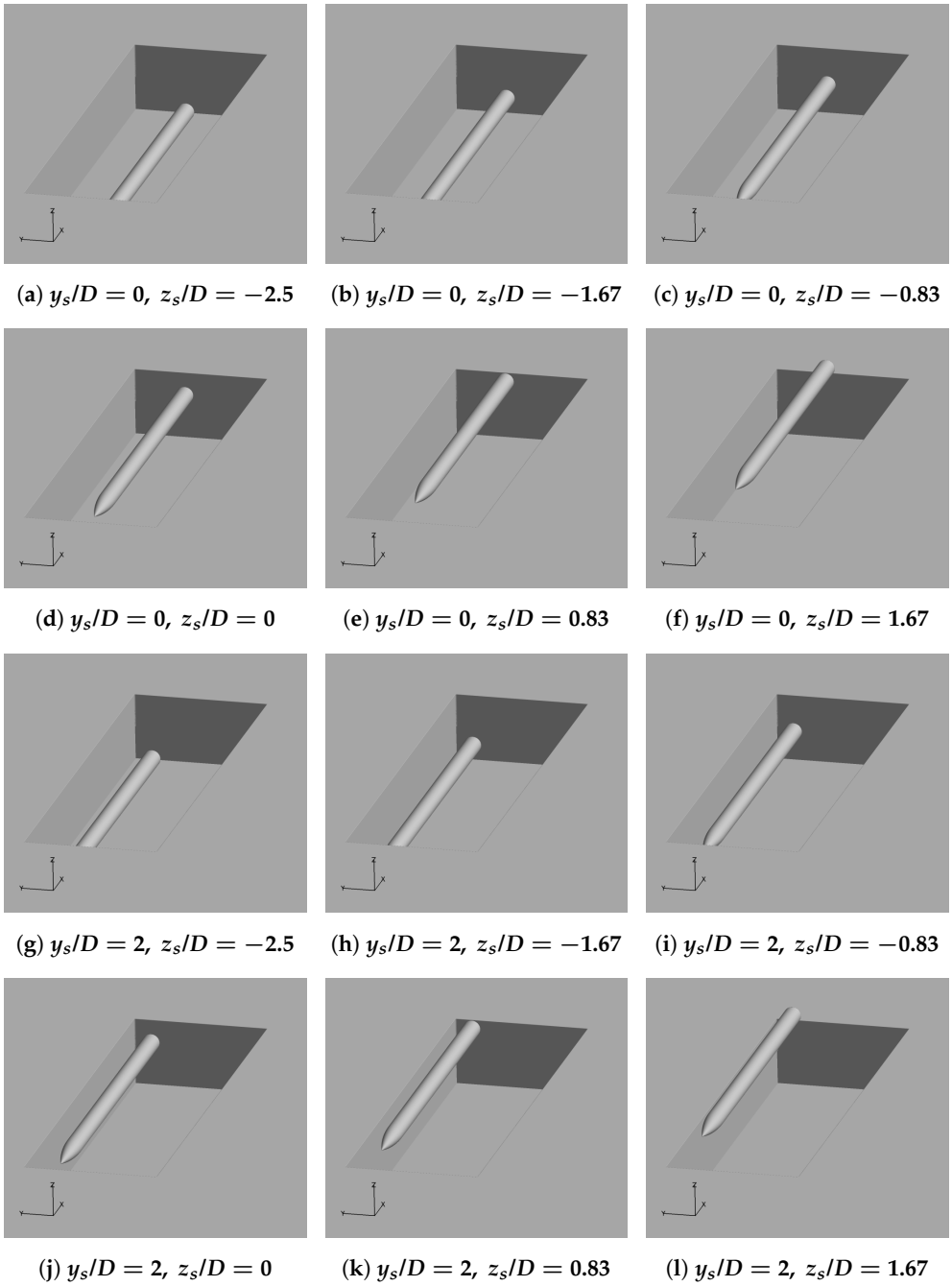

(a) $y_s/D = 0,\ z_s/D = -2.5$ **(b)** $y_s/D = 0,\ z_s/D = -1.67$ **(c)** $y_s/D = 0,\ z_s/D = -0.83$

(d) $y_s/D = 0,\ z_s/D = 0$ **(e)** $y_s/D = 0,\ z_s/D = 0.83$ **(f)** $y_s/D = 0,\ z_s/D = 1.67$

(g) $y_s/D = 2,\ z_s/D = -2.5$ **(h)** $y_s/D = 2,\ z_s/D = -1.67$ **(i)** $y_s/D = 2,\ z_s/D = -0.83$

(j) $y_s/D = 2,\ z_s/D = 0$ **(k)** $y_s/D = 2,\ z_s/D = 0.83$ **(l)** $y_s/D = 2,\ z_s/D = 1.67$

Figure 3. An overview of the cavity-with-store configurations that were simulated.

The instantaneous force and moment vectors exerted on the store are denoted by $\boldsymbol{\mathcal{F}} = [\mathcal{F}_x, \mathcal{F}_y, \mathcal{F}_z]$ and $\boldsymbol{\mathcal{M}} = [\mathcal{M}_x, \mathcal{M}_y, \mathcal{M}_z]$, respectively, where the reference point for calculating the store moments is 337 mm aft of its nose tip. The store's maximum diameter (D) and cross-section area ($A = 730\,\text{mm}^2$) were used to normalize the forces and moments and calculate the instantaneous aerodynamic coefficients, defined by $\boldsymbol{C}_{\boldsymbol{\mathcal{F}}} = \boldsymbol{\mathcal{F}}/(q_\infty A)$ and $\boldsymbol{C}_{\boldsymbol{\mathcal{M}}} = \boldsymbol{\mathcal{M}}/(q_\infty AD)$, where $q_\infty = 0.5 P_\infty \gamma M_\infty^2$ is the dynamic pressure, P_∞ and M_∞ are

the free stream static pressure and Mach number, respectively, and $\gamma = 1.4$ is the heat capacity ratio of air. Based on the definitions above, the instantaneous axial, lateral, and normal force coefficients of the store are denoted by C_x, C_y, and C_z, respectively, where positive force coefficients correspond to the positive direction of the coordinate system (x, y, z). The instantaneous rolling, pitching, and yawing moment coefficients of the store are denoted by Cm_x, Cm_y, and Cm_z, respectively. A positive pitching moment results in a nose-up motion of the store towards the positive z axis (out from the cavity), whereas a positive yawing moment reflects the movement of the store's nose towards the negative y axis. Time-averaged aerodynamic coefficients are marked with an overline (e.g., $\overline{C}_x$).

The store model is meshed using three overlapping grids (see cyan- and black-colored grids in Figure 4a), resulting in a total of 1.65 million nodes. Overall, 12.8 million nodes were solved for each cavity-with-store configuration. As depicted in Figure 4, the size of cells in the store and cavity meshes are matched to achieve optimal spatial accuracy.

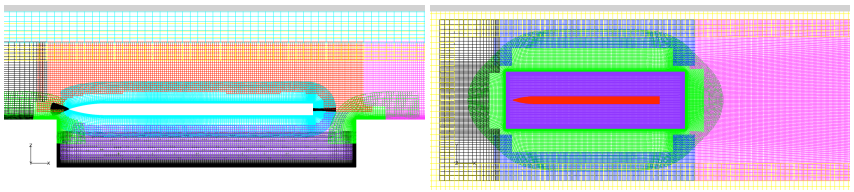

(**a**) (**b**)

Figure 4. An example of the computational domain of the cavity-with-store configuration with the store placed at $(y_s/D, z_s/D) = (0, 0.83)$. (**a**) $y = 0$ plane view; (**b**) upper view.

2.4. Boundary and Flow Conditions

A no-slip boundary condition is applied for both the cavity and the plate walls. The Riemann invariant boundary condition is used for the inflow and outflow boundaries of the computational flow domain; thus, pressure fluctuations and vortical structures can propagate out of the computational domain, not resulting in numerical artifacts due to reflections. The flow simulations were conducted at standard atmosphere sea-level altitude, with a free stream static pressure of $P_\infty = 101{,}325\,\text{Pa}$, Mach number of $M_\infty = 0.4$, and Reynolds number of $Re_L = 7 \times 10^6$. The Mach number was chosen since the focus of this work is on subsonic flow and this is the lowest possible Mach number for which experimental data is available.

2.5. Numerical Procedure

The general numerical procedure consists of initializing the flow field with a steady-state RANS-based simulation and a subsequent time-accurate X-LES k-ω TNT-based simulation. For the convective flux approximation, we used the HLLC (Harten, Lax, and van-Leer) flux difference splitting scheme [43]. The Courant–Friedrichs–Lewy (CFL) value of the mean flow was set to $CFL = 20$ for the empty cavity configuration and $CFL = 10$ for the cavity-with-store configurations. A value of $CFL = 2$ was used for the turbulence model.

For the initial steady-state RANS-based stage, the base k-ω TNT turbulence model was used (2nd order spatial) with a second-order discretization of the mean flow. Approximately 5000 iterations were used for steady-state initialization of the flow until the turbulent boundary layer on the front plate upstream of the cavity developed sufficiently, and a residual drop of four orders of magnitude was achieved. In the subsequent time-accurate X-LES k-ω TNT-based simulation, a second order in time Dual-Time Stepping (DTS) method was applied with a maximum of 30 iterations per time step, with an implicit ADI time marching scheme. For the cavity configurations studied here, we defined a characteristic time for the flow field to pass the cavity, denoted by $\tau = L/U_\infty = 5.5 \times 10^{-3}\,\text{s}$. Given the time scale of τ, a physical time-step of $\Delta t = 1 \times 10^{-4}\,\text{s}$ was used in the simulations to yield a sufficient temporal resolution of the flow field within the cavity configurations. A residual drop of three orders of magnitude for the computational domain was used as a convergence criterion between consecutive time steps. Since the time-accurate stage starts

from the flow solution achieved in the steady-state stage, some period is required for the unsteady flow to develop and fluctuate around a mean value. This value was found here to be 18τ (0.1 s). After this initial period, each simulation ran for 63τ (0.35 s) to collect sufficient data for statistics computation of flow features, as presented in the next section.

3. Results and Discussion

The results obtained for the different cavity configurations are presented here. First, the boundary layer thickness of the incoming flow is analyzed, as well as the time-averaged static pressure coefficient distribution along the cavity floor, to validate the numerical results with existing wind tunnel measurements [4,20]. Next, the flow field within the various cavity configurations is analyzed to shed light on the flow structures that develop in the cavity. Finally, the forces and moments exerted on the store model are computed for each configuration and compared with the experimental results [4].

3.1. Characteristics of the Incoming Boundary Layer

The boundary-layer thickness of the incoming flow plays an important role in the cavity flow mechanism, as previously reported [20,44]. Therefore, to properly resolve the flow field within the cavity model, the incoming turbulent boundary layer thickness at the leading-edge of the (empty) cavity front wall was evaluated and compared to experimental data. Figure 5 depicts the characteristics of the time-averaged turbulent boundary layer profile computed at the centerline of the cavity front wall leading-edge, $(x, y, z) = (0, 0, 0)$. According to the velocity profile computed, a boundary layer thickness (defined for $u/U_\infty = 0.99U_\infty$) of $\delta_{\text{CFD}} = 11$ mm is evaluated, which is in good agreement with the experimental value ($\delta_{\text{EXP}} = 12$ mm) reported by Stallings et al. [4].

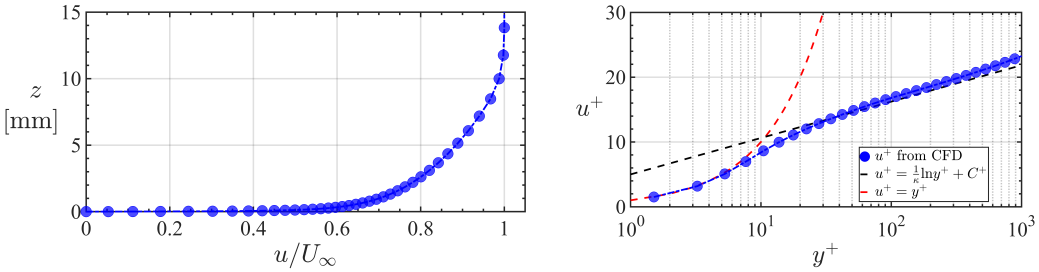

(**a**) (**b**)

Figure 5. Characteristics of the time-averaged boundary layer at the centerline of the (empty) cavity front wall leading-edge, $(x, y, z) = (0, 0, 0)$. (**a**) Boundary layer normalized velocity profile; (**b**) Dimensionless velocity distribution within the boundary layer as a function of the dimensionless wall distance. The logarithmic overlap law ($u^+ = \frac{1}{\kappa}\ln y^+ + C^+$) with $\kappa = 0.41$ and $C^+ = 5.0$ [45], and the pure viscous sublayer asymptote ($u^+ = y^+$) are shown for reference.

3.2. Time-Averaged Static Pressure Coefficient Distribution

Given that the thickness of the incoming turbulent boundary layer is well resolved, the mean static pressure distributions along the floor of the various cavity configurations can now be computed and compared with wind tunnel measurements for further validation of the computational approach. Figure 6 depicts a comparison of the time-averaged static pressure coefficient distribution, $\bar{C}_P(x/L)$, computed along the cavity floor ($y = -W/4$, $z = -H$) with wind tunnel measurements. The static pressure coefficient is defined as $C_P = (P - P_\infty)/q_\infty$, where P is the surface pressure field. The root-mean-square of the pressure coefficient fluctuations is denoted as $C'_{P_{\text{rms}}}$ and its distribution along the cavity floor is highlighted in Figure 6 with a light blue background region. Results are shown both for the empty cavity configuration and the cavity-with-store configurations. Generally, the computed $\bar{C}_P$ distributions along the cavity floor are shown to be in good agreement with available experimental data for all the cavity configurations studied herein. The pressure distributions resemble a transitional flow type, which is expected to form

given the flow conditions and cavity geometry studied [11]. In addition, one may notice significant pressure fluctuations ($C'_{P_{\text{rms}}} > 0.1$) along the cavity floor for $x/L > 0.6$. These large pressure fluctuations are likely a result of the self-sustained oscillations in the shear layer [12], caused by amplification of the shear layer instabilities by the upstream-traveling pressure waves generated at the aft wall by the time-varying impingement of the shear layer. The presence of the store within the cavity is shown to have a somewhat minor effect on the $\bar{C}_P$ distribution and thus the flow type, as also reported by Stallings et al. [4], with the store model only resulting in a slight reduction of the $\bar{C}_P$ values at the aft region of the cavity floor ($0.8 < x/L < 1$).

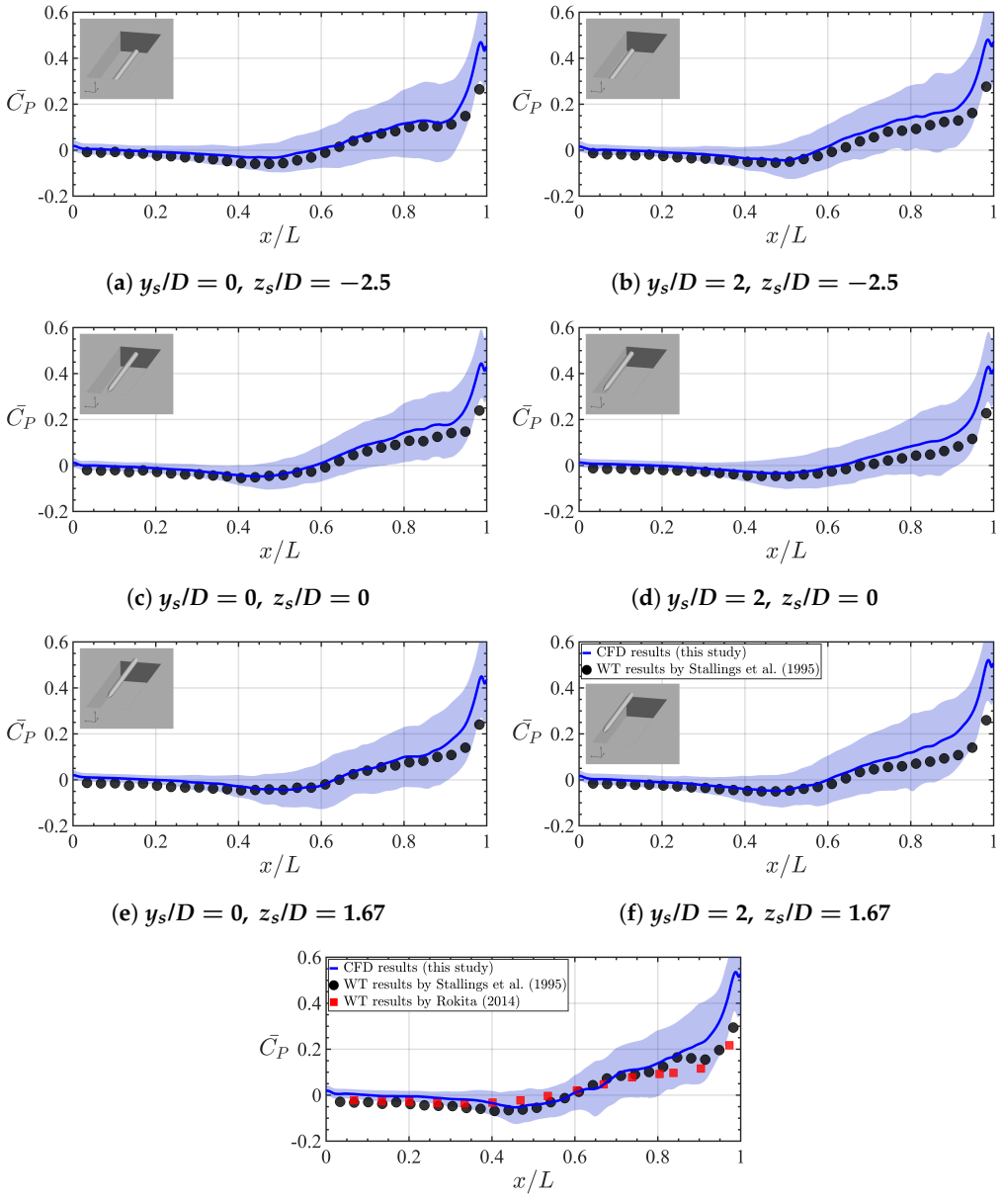

(a) $y_s/D = 0$, $z_s/D = -2.5$ **(b)** $y_s/D = 2$, $z_s/D = -2.5$

(c) $y_s/D = 0$, $z_s/D = 0$ **(d)** $y_s/D = 2$, $z_s/D = 0$

(e) $y_s/D = 0$, $z_s/D = 1.67$ **(f)** $y_s/D = 2$, $z_s/D = 1.67$

(g) Empty cavity

Figure 6. Time-averaged static pressure coefficient distribution, $\bar{C}_P(x/L)$, along the cavity floor ($z = -H$, $y = -W/4$) for the various cavity configurations investigated here. The root-mean-square of the pressure coefficient fluctuations along the cavity floor is highlighted with a light blue background region. Comparison is shown with available wind tunnel results published by Stallings et al. [4] and Rokita [20].

3.3. Flow Characteristics

The flow field within the various cavity configurations studied herein was found to be highly unsteady and three-dimensional, as previously reported in the literature for similar-sized cavities [7,20]. Figure 7 shows an example of the instantaneous pressure coefficient contours ($C_P(\vec{x}, t)$) developed on the cavity floor, the plate surrounding it, and the store model surface. The spatial pressure distribution on the surface and its time evolution demonstrate the unsteady and turbulent flow field within the cavity. The time-varying pressure contour shows a high-pressure region at the aft part of the cavity floor (as shown by Figure 6), an indication of the presence of streamwise vortices forming on the side-edges of the cavity, as well as a low-pressure region on the aft plate. The presence of the store model in the vicinity of the cavity (shown in Figure 7 at $y_s/D = 0$, $z_s/D = 0.83$) is shown to alter the instantaneous surface pressure on the cavity floor, side edges, and aft plate. Such variation in the surface pressure suggests that the store modifies the vortical structures forming within the cavity. However, it seems that the effect of the store presence on the cavity flow field is somewhat masked when analyzing the time-averaged static pressure coefficient distribution along a constant lateral position on the cavity floor; as shown in Figure 6, only minor differences are shown between the empty cavity and cavity-with-store configurations. Therefore, to gain a better insight into the effect of the store model on the flow structures within the cavity, the surface pressure is analyzed on the entire cavity floor, as shown next.

Figure 8 depicts contour maps of the time-averaged static surface pressure coefficient, $\bar{C}_P(x, y)$, computed on the cavity floor for the various cavity configurations studied here. Generally, the presence of the store in the vicinity of the cavity floor ($z_s/D < 0$) is shown to slightly weaken the low-pressure region on the cavity floor (at $0 < x/L < 0.5$), as depicted in Figure 8. In addition, one can notice that positioning the store within the cavity ($z_s/D \leq 0$) and off its centerline ($y_s/D = 2$) strongly affects the lateral pressure distribution on the cavity floor, as depicted by Figure 8b,d,f,h. Moreover, the surface pressure contours depicted in Figure 8 indicate the presence of spanwise flow generated in the aft region of the cavity ($x/L > 0.8$), visualized as strong lateral variation of the surface pressure. The spanwise flow is strongly amplified and progresses upstream when the store is placed within the cavity and off its centerline ($y_s/D = 2$, $z_s/D \leq 0$).

Figure 9 depicts contour maps of the root-mean-square of the static surface pressure coefficient fluctuations, $C'_{P_{\text{rms}}}$, computed on the cavity floor for the various configurations. Generally, the pressure fluctuations on the cavity floor increase along the streamwise direction, where more significant pressure fluctuations are noticeable for $x/L > 0.6$, which agrees with the results in Figure 6. As shown by Figure 9g,h, placing the store model at the height of the separated shear layer ($z_s/D = 0$) seems to significantly reduce the pressure fluctuations on the aft region of the cavity floor ($x/L > 0.8$). When at $z_s/D = 0$, the store was found to interfere with the streamwise convection of vortices shed by the shear layer, resulting in the formation of much smaller vortices; as depicted, for example, by Figure 10, showing the instantaneous vorticity magnitude contour field ($|\vec{\omega}|$) at the center-plane cross-section of the cavity ($y = 0$). This, in turn, reduces the interaction of the streamwise convected vortices with the cavity aft wall, thus resulting in lower pressure fluctuations in the aft region. Such lower pressure fluctuations are likely to diminish the upstream-traveling pressure waves responsible for the self-sustained oscillations in the shear layer, thus damping the acoustic feedback mechanism within the cavity [6]. Moreover, when the store is placed within the cavity ($z_s/D \leq 0$) and off its centerline ($y_s/D = 2$), somewhat lower pressure fluctuations are developed within the cavity, as compared to placing the store at $y_s/D = 0$. When placed at such a lateral position, the store somewhat interferes with the 'two-dimensional' flow field within the cavity, inducing a 'three-dimensional' spanwise flow motion that seems to dampen the interaction with the aft cavity wall and thus reduce the pressure fluctuations and the associated acoustic feedback mechanism. These numerical results are in agreement with experimental results published recently by Ben-Gida [6], where it was shown that placing a store within a jet-fighter's weapons bay

and off its centerline dampens the acoustic feedback mechanism, which is characterized by lower-amplitude Rossiter's modes within the cavity.

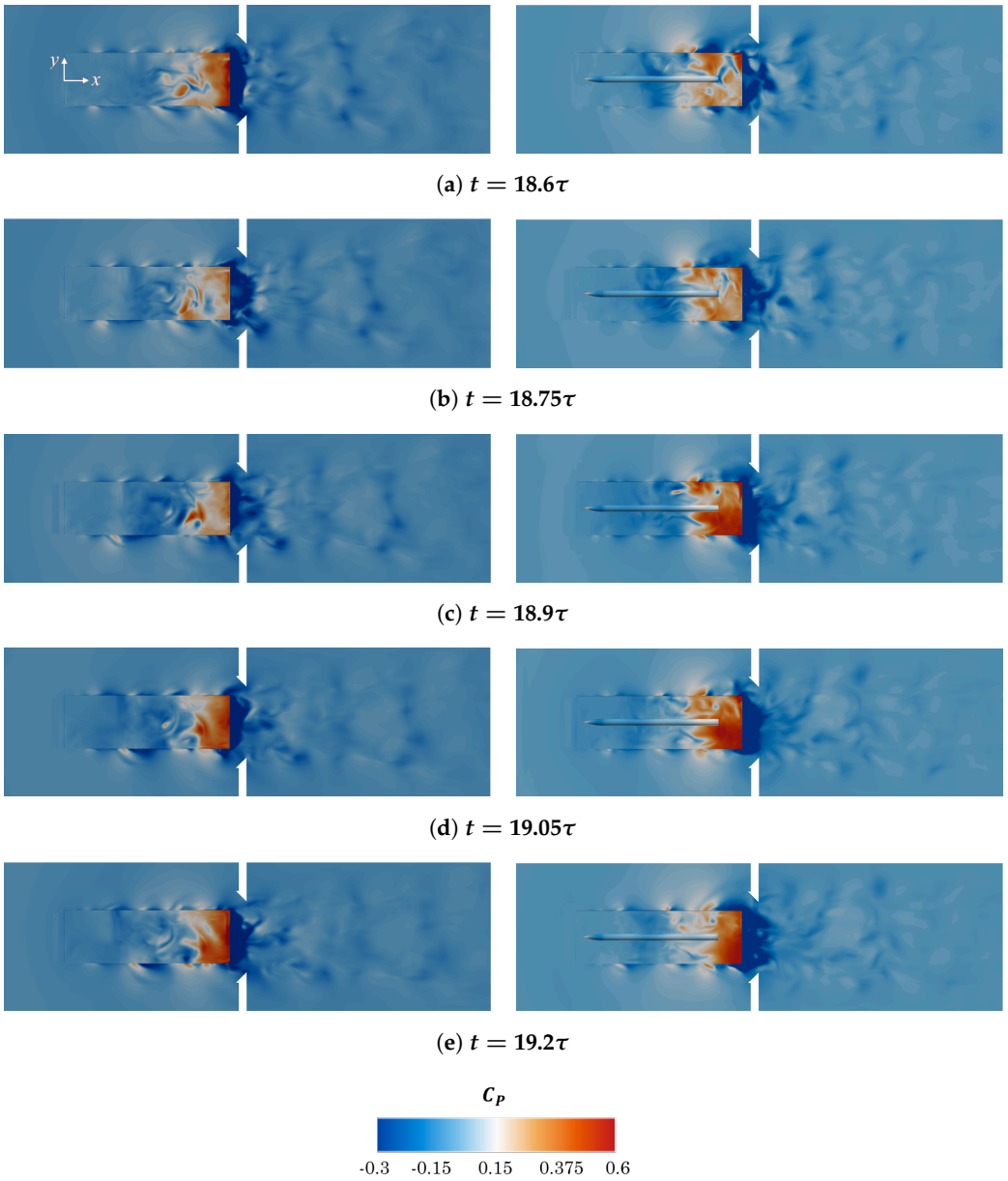

Figure 7. An example of the instantaneous contour maps (shown from above) of the pressure coefficient, $C_P(\vec{x}, t)$, computed on the cavity floor, the plate surrounding it, and the store model surface. Comparison is shown between an empty cavity configuration (**left** column) and the cavity-with-store configuration with the store placed at $(y_s/D, z_s/D) = (0, 0.83)$ (**right** column).

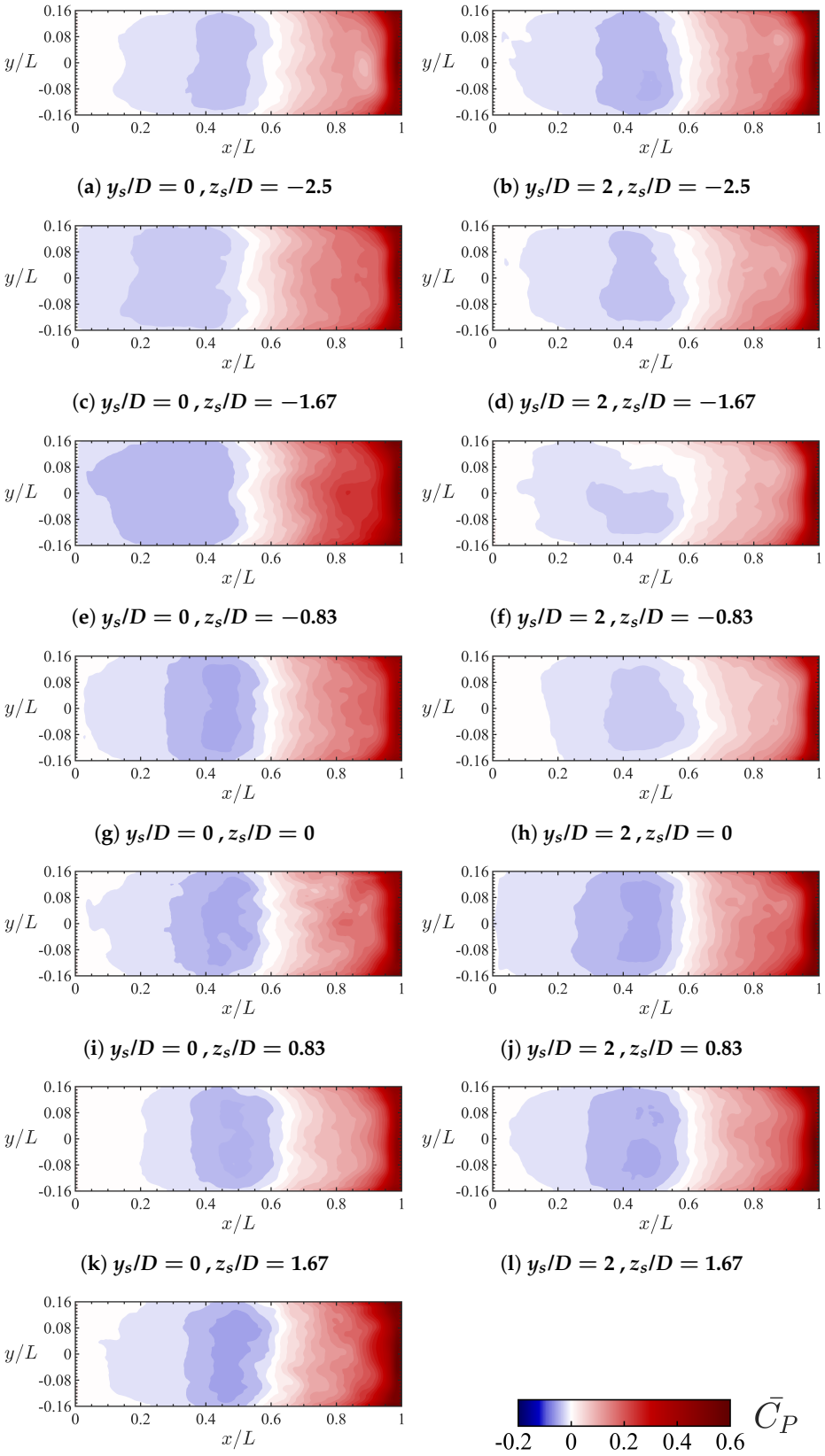

(a) $y_s/D = 0$, $z_s/D = -2.5$ **(b)** $y_s/D = 2$, $z_s/D = -2.5$

(c) $y_s/D = 0$, $z_s/D = -1.67$ **(d)** $y_s/D = 2$, $z_s/D = -1.67$

(e) $y_s/D = 0$, $z_s/D = -0.83$ **(f)** $y_s/D = 2$, $z_s/D = -0.83$

(g) $y_s/D = 0$, $z_s/D = 0$ **(h)** $y_s/D = 2$, $z_s/D = 0$

(i) $y_s/D = 0$, $z_s/D = 0.83$ **(j)** $y_s/D = 2$, $z_s/D = 0.83$

(k) $y_s/D = 0$, $z_s/D = 1.67$ **(l)** $y_s/D = 2$, $z_s/D = 1.67$

(m) Empty cavity

Figure 8. Contour maps of the time-averaged static surface pressure coefficient, $\bar{C_P}(x, y)$, computed on the cavity floor for the various cavity configurations. The flow is from left to right.

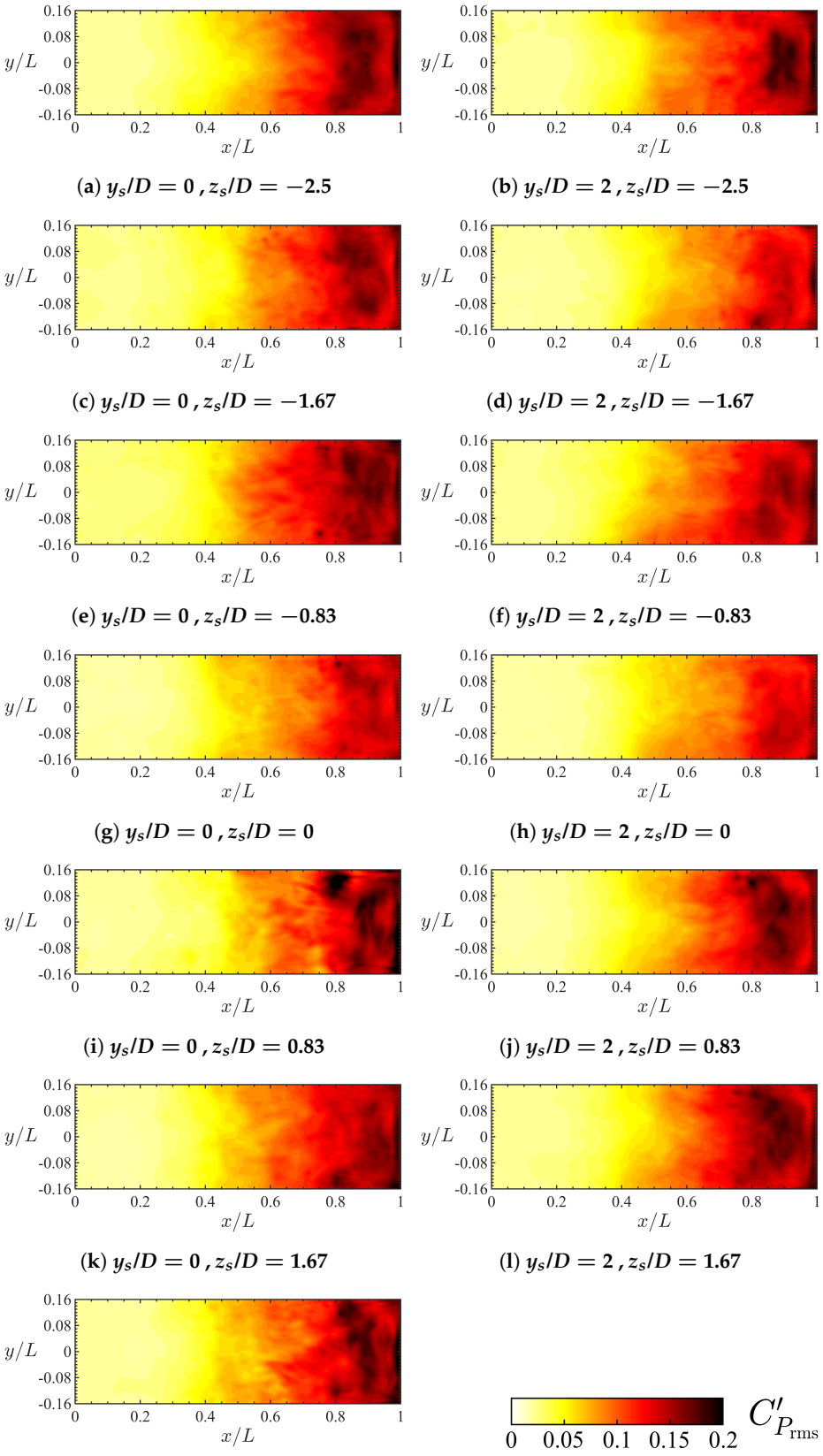

(a) $y_s/D = 0$, $z_s/D = -2.5$ **(b)** $y_s/D = 2$, $z_s/D = -2.5$

(c) $y_s/D = 0$, $z_s/D = -1.67$ **(d)** $y_s/D = 2$, $z_s/D = -1.67$

(e) $y_s/D = 0$, $z_s/D = -0.83$ **(f)** $y_s/D = 2$, $z_s/D = -0.83$

(g) $y_s/D = 0$, $z_s/D = 0$ **(h)** $y_s/D = 2$, $z_s/D = 0$

(i) $y_s/D = 0$, $z_s/D = 0.83$ **(j)** $y_s/D = 2$, $z_s/D = 0.83$

(k) $y_s/D = 0$, $z_s/D = 1.67$ **(l)** $y_s/D = 2$, $z_s/D = 1.67$

(m) Empty cavity

Figure 9. Contour maps of the root-mean-square of the static surface pressure coefficient fluctuations, $C'_{P_{\mathrm{rms}}}$, computed on the cavity floor for the various cavity configurations. The flow is from left right.

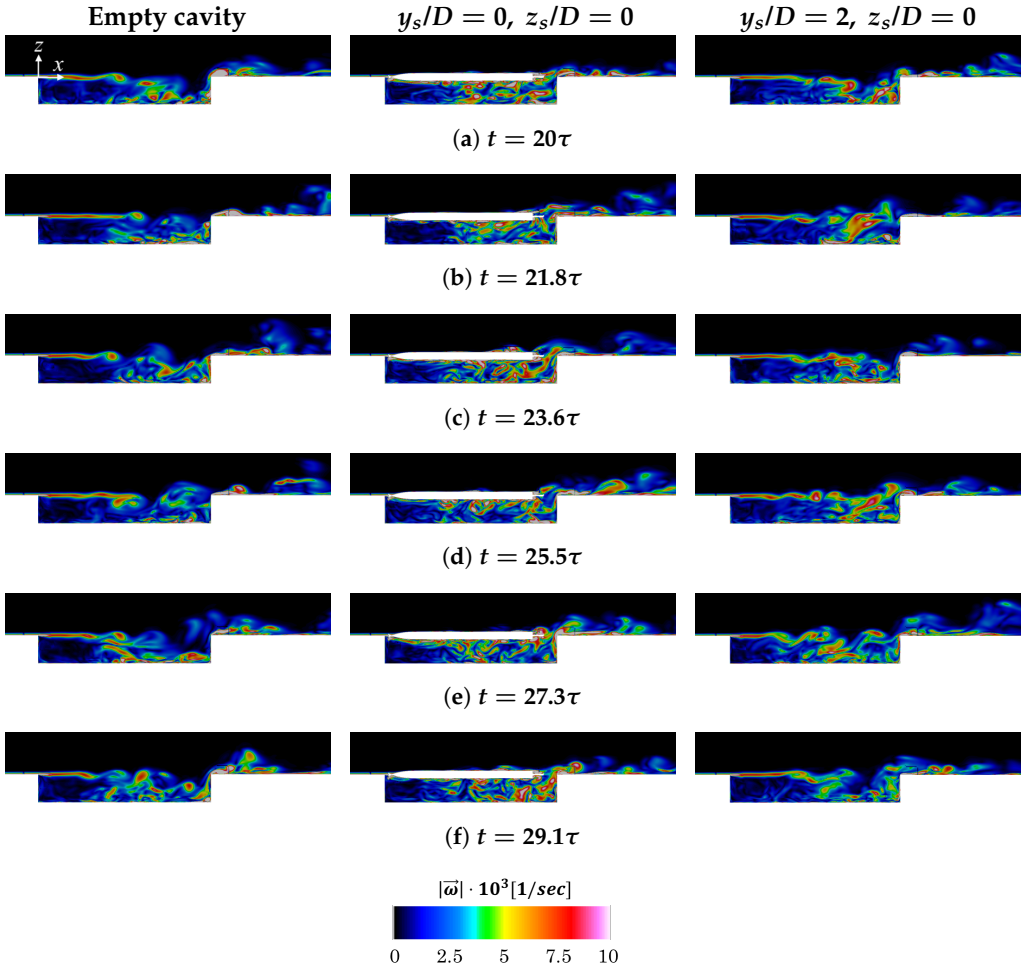

Figure 10. Instantaneous vorticity magnitude contour fields, $|\vec{\omega}|$, at the center-plane cross-section of the cavity ($y = 0$). Comparison is shown between an empty cavity configuration (**left** column) and two cavity-with-store configurations: $y_s/D = 0,\ z_s/D = 0$ (**middle** column) and $y_s/D = 2,\ z_s/D = 0$ (**right** column).

To further investigate the effect of the store position on the acoustic feedback mechanism within the cavity, the overall sound pressure level (OASPL) is computed on the cavity floor of the various configurations studied here, accordingly:

$$OASPL = 20\log_{10}\frac{P'_{\text{rms}}}{P_{\text{ref}}}, \tag{15}$$

where P'_{rms} is the root-mean-square of the pressure fluctuations and P_{ref} is the threshold of human hearing (=20 μPa). Figure 11 depicts a comparison of the mean OASPL distribution (averaged along the lateral direction) along the cavity floor between an empty cavity and various cavity-with-store configurations. In agreement with the contour maps of the pressure fluctuations (see Figure 9), the OASPL is shown to increase along the cavity floor, with values as high as 160 dB at the aft region. Generally, the OASPL trend and the range of values seem to agree with previously published results [12,20]. Compared to the empty cavity configuration, it is shown that placing the store at $z_s/D = 0$, where the shear layer is, results in up to 2.5 dB reduction of the OASPL along the cavity floor. Moreover, placing the store within the cavity ($z_s/D \leq 0$) and off its centerline ($y_s/D = 2$) results in similar or slightly higher OASPL reduction. These OASPL trends demonstrate effect of the store position on damping the acoustic feedback mechanism within the cavity; when placed at $z_s/D = 0$, the store interferes with the self-sustained oscillations in the shear layer,

and when placed laterally ($y_s/D = 2$) and within the cavity ($z_s/D \leq 0$) the store induces spanwise flow that damps the flow interaction with the aft cavity wall.

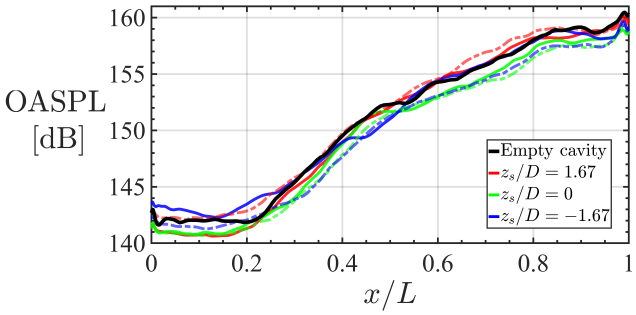

Figure 11. Comparison of the mean OASPL distribution (averaged along the lateral direction, y) along the cavity floor between an empty cavity and various cavity-with-store configurations. Solid ('-') colored curves correspond to configurations with the store placed at the cavity centerline ($y_s/D = 0$), whereas dashed ('- -') colored curves correspond to configurations with the store placed off the cavity centerline ($y_s/D = 2$).

The time-averaged streamlines colored with the velocity magnitude, U, are used to visualize the mean flow structures that develop within the baseline empty cavity configuration, as depicted in Figure 12. Generally, the flow field within cavities such as the one studied herein is reasonably organized in the front cavity region. However, due to the Kelvin–Helmholtz instability in the shear layer, a complex, more chaotic flow field is developed in the cavity, involving a large re-circulation zone occupying most of the cavity volume, two spanwise vortices close to the cavity floor (both in the front and aft regions of the cavity), and strong trailing vortices that shed from the side walls of the cavity and interact with the vortices shed from the cavity aft wall [46]. The above-mentioned flow structures can be visually identified from time-averaged streamlines shown in Figure 12. The large re-circulation zone within the empty cavity is depicted at $0.3 \leq x/L \leq 0.75$, the two spanwise vortices on the cavity floor are visible, one at the front ($x/L \leq 0.1$) and another at the aft region ($x/L > 0.8$), and the energized trailing vortices shed from the cavity side walls can be identified. The position of the large re-circulation zone within the empty cavity seems to agree with the low-pressure region depicted in the time-averaged static surface pressure contour in Figure 8m. In addition, the location of the aft spanwise vortex ($x/L > 0.8$) agrees well with the region of strong lateral variation of the surface pressure on the cavity floor, as shown in Figure 8m, thus supporting the argument that the lateral variation of the surface pressure is a manifestation of the aft spanwise vortex [46]. Moreover, one may note a strong correlation between the rise of the pressure fluctuations along the cavity floor (see Figure 9m) and the position of both the re-circulation zone and the aft spanwise vortex. The aft spanwise vortex, in particular, appears to be associated with the most significant pressure fluctuations on the cavity aft floor ($C'_{P_{\text{rms}}}$), implying its highly unsteady nature as compared to the more 'stationary' re-circulation zone.

The effect of the store model on the time-averaged streamlines within the cavity is shown in Figure 13 for various configurations. Generally, the presence of the store within the cavity ($z_s/D < 0$) results in a distortion of both the re-circulation zone and the aft spanwise vortex (located close to the cavity floor), where both vortical regions appear less organized as the store is placed closer to the cavity floor. This observation supports the diminished low-pressure region observed on the cavity floor (see Figure 8) and the slightly reduced pressure at the aft region (see Figure 6). In addition, as the store is placed closer to the cavity floor, an amplified interaction is depicted between the streamwise vortices forming on the cavity side walls and the trailing vortices shed from the aft region of the cavity. This phenomenon is presumed to be due to the alteration of the re-circulation zone and aft spanwise vortex by the store, which can induce stronger lateral flow motion that can amplify the streamwise vortices shed from the side walls of the cavity. Surprisingly, the

front spanwise vortex (located close to the cavity floor) is shown to be somewhat unaffected by the store's presence within the cavity. It is noteworthy that similar results were found for a relatively larger diameter store within a cavity of similar size [5,6].

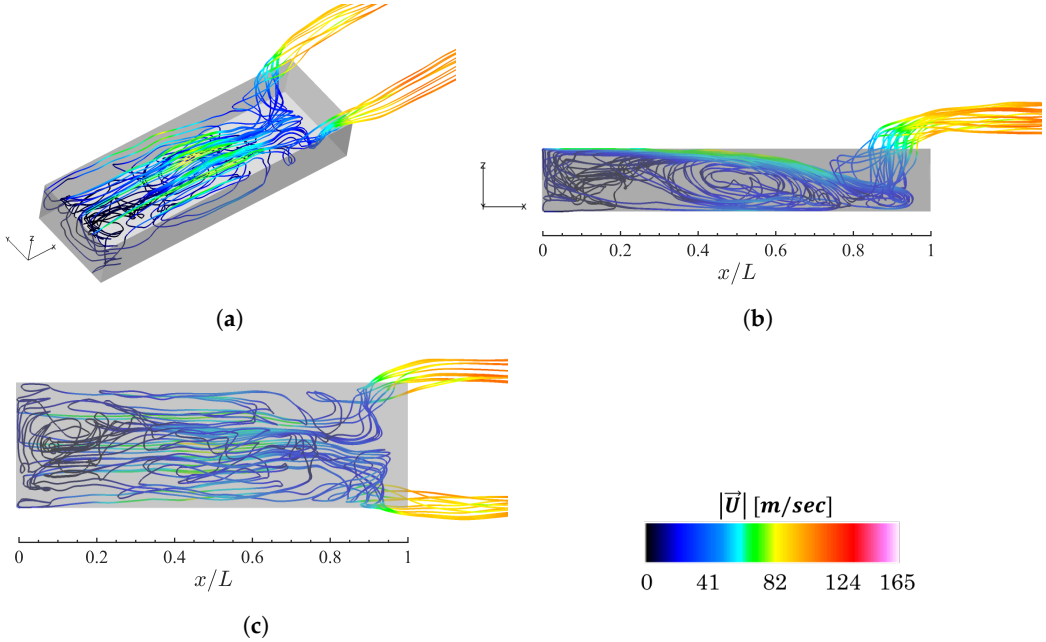

Figure 12. Time-averaged streamlines, colored with the velocity magnitude (U), within the empty cavity configuration. (**a**) Isometric view; (**b**) xz plane side view; (**c**) xy plane bottom view.

When the store is placed within the cavity ($z_s/D \leq 0$) and off its centerline ($y_s/D = 2$), the symmetry of the time-averaged flow field within the cavity (around the centerline) breaks, leading to asymmetrical flow field, as depicted in Figure 13b,d. This observation agrees with surface pressure contours on the cavity floor (see Figure 8), which show that the laterally-positioned store induces a large lateral variation of the pressure field. Similarly to the flow field results shown for a store placed at the cavity centerline ($y_s/D = 0$), placing the store within the cavity ($z_s/D \leq 0$) and at $y_s/D = 2$ results in a significant modification of both the re-circulation zone and the aft spanwise vortex, as well as amplified interaction between the streamwise vortices on the cavity side walls and the trailing vortices shed from the aft region. In particular, the aft spanwise vortex is strongly amplified and progresses upstream when the store is placed within the cavity and off its centerline ($y_s/D = 2$, $z_s/D \leq 0$), which is in agreement with the surface pressure results (see Figure 8). The asymmetrical flow field induced by the laterally-placed store appears to be responsible for the damped interaction with the aft cavity wall (see Figure 9) and the lower OASPL in the cavity (see Figure 11).

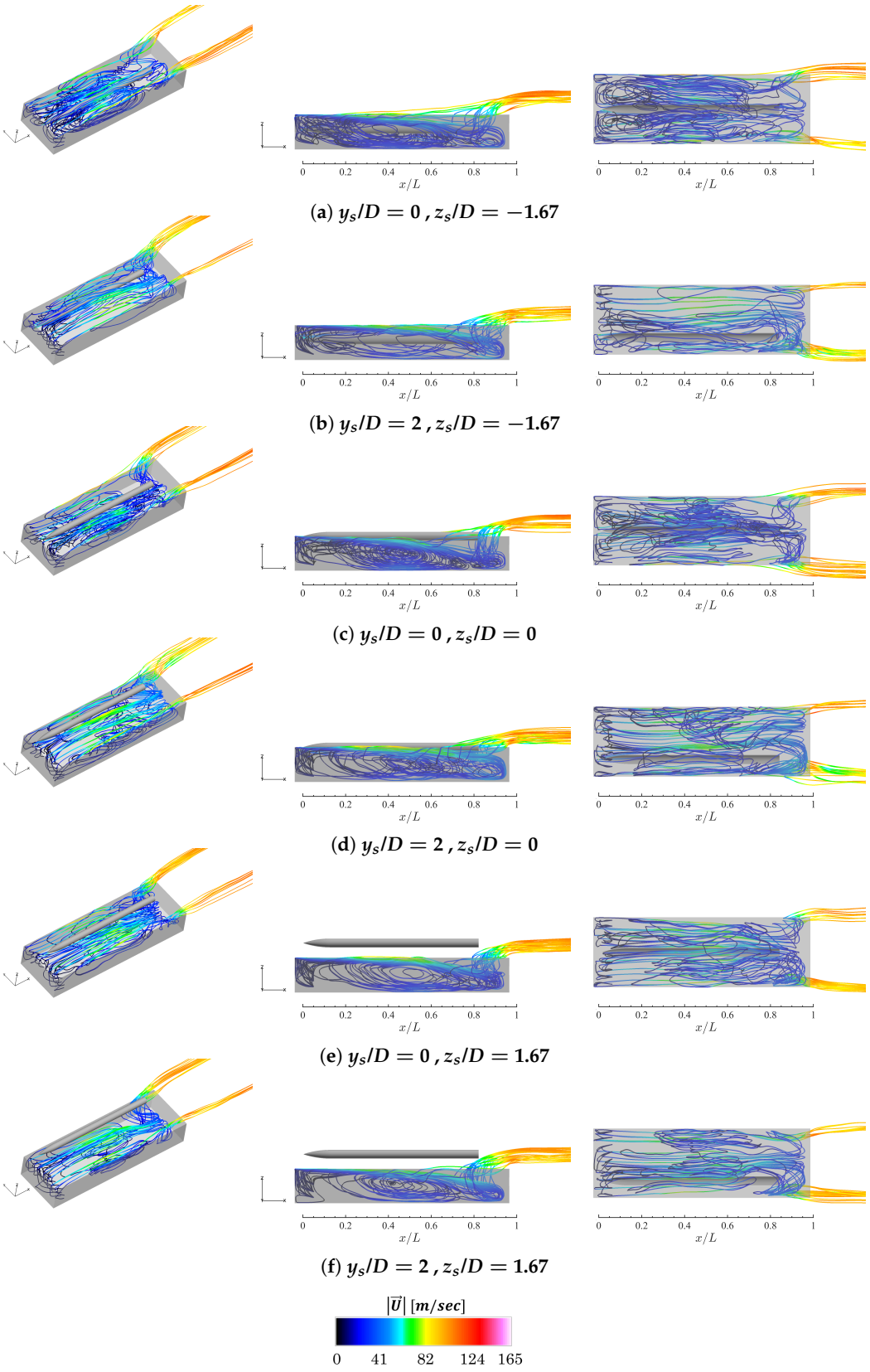

Figure 13. Time-averaged streamlines, colored with the velocity magnitude (U), within various cavity-with-store configurations. Each row includes isometric, xz plane, and xy plane (bottom) views.

3.4. Forces and Moments

As shown in previous sections, introducing a store model into the cavity is shown to have a distinct effect on the pressure fluctuations and the time-averaged flow structures that develop within the cavity. As a result, one should expect the forces and moments exerted on the store to vary as well, depending on its location with respect to the cavity floor. Figure 14 depicts an example of the time variation of the instantaneous aerodynamic coefficients for a store model placed at $y_s/D = 2$, $z_s/D = 0$. The time-dependent results are shown from $t = 18.2\tau$ to $t = 85\tau$, after the initial period given for the unsteady flow to develop. Each aerodynamic coefficient was averaged over the corresponding time period to yield a time-averaged value. As depicted in Figure 14, each of the store's instantaneous aerodynamic coefficients fluctuate in time around a time-averaged value (marked as red lines), where the light red background regions correspond to the root-mean-square of the aerodynamic coefficients' fluctuations. It is worth noting that the store model has no canards, wings, or fins. Therefore, the rolling moment coefficient of the store model is not shown; its value was found to be significantly smaller ($Cm_x \sim \mathcal{O}(10^{-3})$) compared to the other coefficients for all the cavity configurations studied here. Generally, the instantaneous aerodynamic coefficients are characterized by large amplitude fluctuations, particularly the pitching and yawing moment coefficients, caused by the unsteady turbulent flow field within the cavity. Kim et al. [21], who investigated a store placed at the cavity shear layer region, reported similar fluctuations of the aerodynamic coefficients. As shown in Figure 14, the fluctuations of the pitching moment can be large enough to cause repeatable sign-alteration of the coefficient; i.e., the store model can experience large pitch-up and pitch-down moments, which can potentially lead to major challenges in ensuring safe store separation from the cavity.

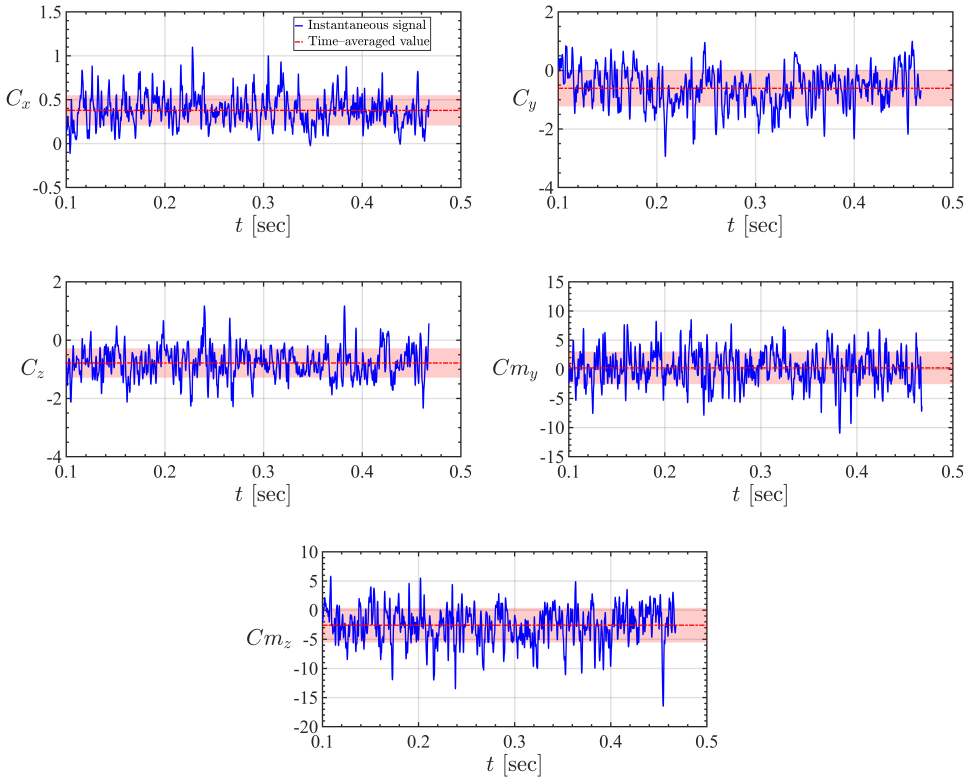

Figure 14. Time variation of the instantaneous aerodynamic coefficients of the store model, when placed at $(y_s/D, z_s/D) = (2, 0)$. The light red background regions correspond to the root-mean-square of the instantaneous time-dependent aerodynamic coefficients computed from the CFD simulations. Time-averaged values are shown as red lines.

Figure 15 depicts the variation of the time-averaged aerodynamic coefficients with the normal position of the store within the cavity (z_s/D) for the two lateral positions investigated here ($y_s/D = 0$ and $y_s/D = 2$). It should be noted that the time-averaged aerodynamic coefficients are marked here with an overline (e.g., $C\bar{m}_y$). The light blue/red background regions correspond to the root-mean-square of the aerodynamic coefficients' fluctuations computed for each store position (y_s, z_s). A comparison is presented with available wind tunnel results (black curves) published by Stallings et al. [4], where the error bars indicate the uncertainty of the experimental data. Overall, a good agreement is shown between the numerical results presented here and the wind tunnel data [4], given the fluctuating nature of the aerodynamic forces and moments exerted on the store and the experimental uncertainty. Generally, the aerodynamic coefficients exhibit a distinct and non-linear dependency in the store normal position (z_s/D), which is further pronounced when the store is placed at $y_s/D = 2$. Specifically, the most significant variation in the aerodynamic coefficients occurs when the store is placed within the cavity ($z_s/D \leq 0$). This finding aligns with the time-averaged streamline patterns observed in Figure 13, where the store presence within the cavity was shown to alter the flow structures. In particular, the aerodynamic forces exerted on the store exhibit a stronger non-linear variation with z_s/D than the pitching and yawing moments, which agrees with experimental results published by Ben-Gida [6] on a cavity of similar size.

Numerical results reveal that the time-averaged axial force coefficient ($\bar{C}_x$) decreases non-linearly as the store is closer to the cavity floor. This is due to the low-velocity flow field within the cavity (see Figure 13). One can notice the store model experiences a negligible axial force ($\bar{C}_x \sim 0$) when located deep within the cavity, at $z_s/D = -2.5$. The time-averaged lateral force coefficient ($\bar{C}_y$) is shown to be somewhat negligible when the store is placed at $y_s/D = 0$, regardless of the store's normal position. When the store is positioned within the cavity ($z_s/D \leq 0$) and off its centerline ($y_s/D = 2$), the time-averaged lateral force is shown to be primarily negative, resulting an inward-force that pulls the store towards the cavity centerline, with significant non-linear dependency in z_s/D. This finding is in agreement with the large lateral variations the store induces on the flow field within the cavity, as depicted by Figures 8 and 13. It should be noted that $\bar{C}_y$ approaches a zero value as the store is located deep within the cavity or far out from it, presumably because of the weak lateral motion in these limits. The time-averaged normal force coefficient ($\bar{C}_z$) is shown to decrease in magnitude as the store is positioned closer to the cavity floor, where the lateral position of the store appears to have a negligible effect. It is noteworthy that a similar trend was indicated by Ben-Gida [6] with a much larger store model. The maximum absolute $\bar{C}_z$ value appears to develop when the store is at the height of the shear layer ($z_s/D = 0$), which results in a significant down-force that pulls the store into the cavity.

The computed time-averaged pitching moment coefficient ($C\bar{m}_y$) is shown to be mostly positive for the different store positions within the cavity, indicating a pitch-up motion (out from the cavity) is exerted on the store. However, the large amplitude fluctuations of the pitching moment coefficient, as indicated in Figure 15, are such that, instantaneously, the store can experience significant pitch-up and pitch-down motions; thus, demonstrating the store separation challenge from associated with cavity studied here. Similar to the lateral force coefficient, when the store is placed at $y_s/D = 0$, the time-averaged yawing moment coefficient ($C\bar{m}_z$) is shown to be relatively small and unaltered by the store's normal position. The time-averaged yawing moment coefficient is shown to be relatively large in magnitude when the store is positioned in the vicinity of the shear layer height ($0.85 \leq z_s/D \leq -0.85$) and off the cavity centerline ($y_s/D = 2$), resulting in a significant yaw-out motion of the store leading-edge towards the cavity right side wall (out from the centerline). Similarly to the pitching moment, the yawing moment coefficient is characterized by large amplitude fluctuations such that the store can instantaneously experience significant yaw-out and yaw-in motions that can impose challenges to a safe store separation.

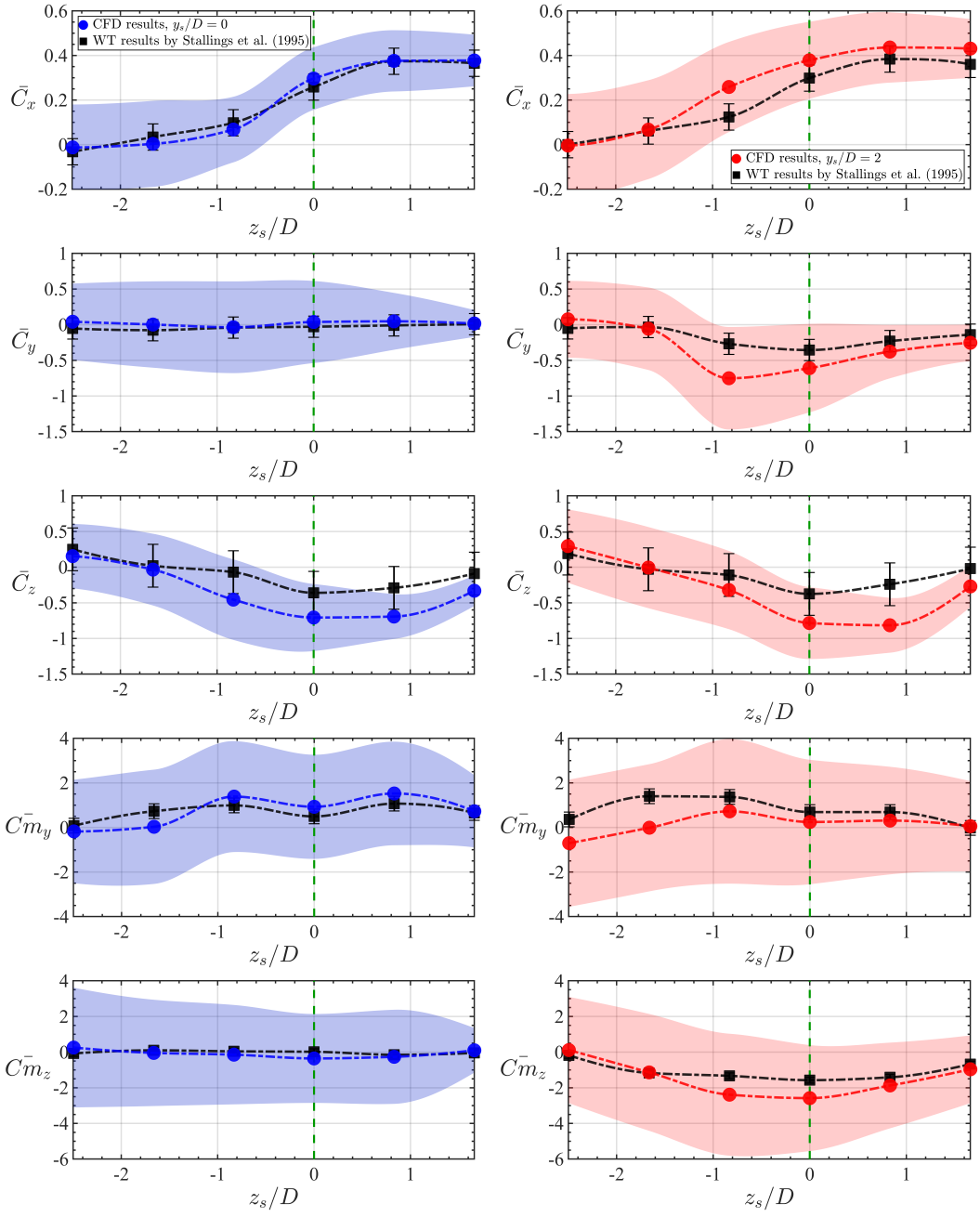

(a) $y_s/D = 0$ **(b)** $y_s/D = 2$

Figure 15. Variation of the time-averaged aerodynamic coefficients of the store with its normal position within the cavity (z_s/D). The results in the left column correspond to configurations with the store placed at the cavity centerline ($y_s/D = 0$), whereas the results in the right column correspond to configurations with the store placed off the cavity centerline ($y_s/D = 2$). The light blue/red background regions correspond to the root-mean-square of the aerodynamic coefficients' fluctuations computed from the CFD simulations for each store position (y_s, z_s). Comparison is shown with available wind tunnel aerodynamic data (black curves) taken by Stallings et al. [4]. The error bars (in black) depict the uncertainty of the wind tunnel aerodynamic data.

4. Conclusions

In this study, three-dimensional, subsonic ($M_\infty = 0.40$), and time-accurate numerical flow simulations are performed using the EZNSS CFD code with X-LES k-ω TNT modeling to characterize the unsteady flow field within NASA's benchmark rectangular cavity with a store model. The investigated cavity had a length-to-height ratio of $L/H = 6.25$ and a width-to-height ratio of $W/H = 2$. A total of twelve cavity-with-store configurations were studied, with the store placed at two lateral locations ($y_s/D = 0$ and $y_s/D = 2$) and at six different normal positions ($z_s/D = [-2.5, -1.67, -0.85, 0, 0.85, 1.67]$).

Generally, the numerical results presented here are in good agreement with available relevant experimental data [4–6,12,20,21], both in terms of the time-averaged pressure coefficient distributions along the cavity floor ($\bar{C_P}(x/L)$) and in terms of the time-averaged aerodynamic coefficients. Results show that the store's effect on the cavity flow field is somewhat masked when analyzing the time-averaged static pressure coefficient distribution along a constant lateral position on the cavity floor. Therefore, in this study, the surface pressure contours on the cavity floor and the time-averaged streamlines are also analyzed, revealing a more complex interaction between the store and the flow field within the cavity.

The time-averaged flow field visualization within the cavity revealed that the flow is reasonably organized in the front region, while a chaotic flow field develops as the shear layer breaks downstream, involving a large re-circulation zone, a spanwise vortex at the aft cavity region, and energized trailing vortices that shed from the cavity aft wall. A strong correlation is found between the rise of the pressure fluctuations along the cavity floor and the positions of the re-circulation zone and the aft spanwise vortex. The highly unsteady behavior of the aft spanwise vortex, in particular, appears to be responsible for the large amplitude pressure fluctuations on the cavity aft floor, yielding an OASPL of up to 160 dB.

The position of the store within the cavity is shown to have an important role in damping the acoustic feedback mechanism within the cavity. When placed at $z_s/D = 0$, the store interferes with the self-sustained oscillations in the shear layer, resulting in up to 2.5 dB reduction of the OASPL on the cavity floor. Similar or slightly higher OASPL reduction was found on the cavity floor when the store is placed laterally ($y_s/D = 2$) and within the cavity ($z_s/D \leq 0$). When at these positions, the store induces a strong spanwise flow motion that distorts the re-circulation zone and amplifies the aft spanwise vortex, thus diminishing the flow interaction with the aft cavity wall, which is responsible for the self-sustained oscillations in the shear layer.

The complex interaction of the store model and the cavity flow field is manifested by the instantaneous loads exerted on the store, which are characterized by large amplitude fluctuations, such that the store can instantaneously experience repeatable sign-alternating forces/moments; thus demonstrating the significant challenges involved in ensuring safe store separation from cavities. The time-averaged aerodynamic coefficients are shown to have a distinct non-linear variation with the store normal position (z_s/D), which is further pronounced when the store is placed laterally ($y_s/D = 2$) and within the cavity ($z_s/D \leq 0$), presumably due to the spanwise flow induced by the store. In particular, the largest aerodynamic loads (in magnitude) are found to exert on the store when it is positioned in the vicinity of the shear layer height ($0.85 \leq z_s/D \leq -0.85$). Longitudinally, when placed within the cavity ($z_s/D \leq 0$), the store experiences an overall down-force and a pitch-up moment. When the store is laterally placed within the cavity, an inward-force and a significant yaw-out moment are also accompanied.

The findings presented in this study can serve as the basis for developing efficient and more accurate computational schemes for resolving the flow field in cavity-with-store configurations. Moreover, the interaction between the generic store model and the turbulent flow field within the rectangular cavity, as studied herein, can be further expanded to more challenging flow regimes (e.g., transonic/supersonic) and real-world cavity geometries that include doors and multiple stores. Such efforts hold great promise for improving current aero-mechanical certification procedures of weapons bays store separation by applying validated computational methodologies.

Funding: This research received no external funding.

Data Availability Statement: Not applicable.

Acknowledgments: The author would like to thank the professional support given by Yair Mor-Yossef and Motti Adar throughout different stages of this study.

Conflicts of Interest: The author declares no conflict of interest.

Abbreviations

The following abbreviations are used in this manuscript:

CFD	Computational Fluid Dynamics
DES	Detached Eddy Simulation
DNS	Direct Numerical Simulation
IDDES	Improved Delayed Detach-Eddy Simulation
LES	Large Eddy Simulatios
JDAM	Joint Direct Attack Munition
PIV	Particle Image Velocimetry
PSP	Pressure-Sensitive Paint
RANS	Reynolds-Averaged Navier–Stokes
S–A	Spalart–Allmaras
SGS	Sub-Grid-Scale
TNT	Turbulent/Non-Turbulent
URANS	Unsteady Reynolds Averaged Navier–Stokes
X-LES	Extra-Large-Eddy Simulation

References

1. Johnson, R.A.; Stanek, M.J.; Grove, J.E. Store separation trajectory deviations due to unsteady weapons bay aerodynamics. In Proceedings of the 46th AIAA Aerospace Sciences Meeting and Exhibit, Reno, NV, USA, 7–10 January 2008.
2. Westmoreland, W.S. Trajectory variation due to an unsteady flow-field. In Proceedings of the 47th AIAA Aerospace Sciences Meeting, Oralndo, FL, USA, 5–8 January 2009.
3. Stallings, R.L.; Forest, D.K. *Separation Characteristics of Internally Carried Stores at Supersonic Speeds*; NASA TP–2993; NASA: Washington, DC, USA, 1990.
4. Stallings, R.L.; Plentovich, E.B.; Tracy, M.B.; Hemsch, M.J. *Measurements of Store Forces and Moments and Cavity Pressures for a Generic Store in and near a Box Cavity at Subsonic and Transonic Speeds*; NASA TM–4611; NASA: Washington, DC, USA, 1995.
5. Ben-Gida, H. Experimental study of the transonic flow within a jet-fighter weapons bay with internal stores. In Proceedings of the AIAA Aviation Forum, Chicago, IL, USA & Virtual , 27 June–1 July 2022.
6. Ben-Gida, H. Experimental study of an air-to-ground store release from a jet-fighter weapons bay in Transonic flow conditions. In Proceedings of the AIAA AVIATION Forum, San Diego, CA, USA and Online , 12–16 June 2023.
7. Lawson, S.J.; Barakos, G.N. Review of numerical simulations for high-speed, turbulent cavity flows. *Prog. Aerosp. Sci.* **2011**, *47*, 186–216. [CrossRef]
8. Charwat, A.F.; Roos, J.N.; Dewey, C.F.; Hiltz, J.A. An investigation of separated flows, part II, Flow in the cavity and heat transfer. *J. Aerosp. Sci.* **1961**, *28*, 457–470. [CrossRef]
9. Rossiter, J. *The Effects of Cavities on the Buffetting of Aircraft*; Technical Memorandum AERO.754; Royal Aircraft Establishment: Farnborough, UK, 1962.
10. Tracy, M.B.; Plentovich, E.B. *Characterization of Cavity Flow Fields Using Pressure Data Obtained in the Langley 0.3-Meter Transonic Cryogenic Tunnel*; NASA TM–4436; NASA: Washington, DC, USA, 1993.
11. Plentovich, E.B.; Stallings, R.L.; Tracy, M.B. *Experimental Cavity Pressure Measurements at Subsonic and Transonic Speeds*; NASA TP–3358; NASA: Washington, DC, USA, 1993.
12. Tracy, M.B.; Plentovich, E.B. *Cavity Unsteady-Pressure Measurements at Subsonic and Transonic Speeds*; NASA TP–3669; NASA: Washington, DC, USA, 1997.
13. Hamed, A.; Basu, D.; Das, K. Effect of Reynolds number on the unsteady flow and acoustic fields of supersonic cavity. In Proceedings of the Fourth ASME/JSME Joint Fluids Engineering Conference, Honolulu, HI, USA, 6–10 July 2003.
14. Rizzetta, D. Numerical simulation of supersonic flow over a three-dimensional cavity. *AIAA J.* **1988**, *26*, 799–807. [CrossRef]
15. Spalart, P. Strategies for turbulence modeling and simulations. *Int. J. Heat Fluid Flow* **2000**, *21*, 252–263. [CrossRef]
16. Mendonça, F.; Allen, R.; de Charentenay, J.; Kirkham, D. CFD prediction of narrow band and broadband cavity acoustics at M=0.85. In Proceedings of the In 9th AIAA/CEAS Aeroacoustic Conference Exhibition, Hilton Head, SC, USA, 12–14 May 2003.
17. Rizzetta, D.P.; Visbal, M.R. Large-eddy simulation of supersonic cavity flow-fields including flow control. *AIAA J.* **2003**, *41*, 1452–1462. [CrossRef]

18. Viswanathan, A.K.; Squires, K.D.; Forsythe, J.R. Detached eddy simulation of the flow over an axisymmetric cavity. In Proceedings of the 41th AIAA Aerospace Sciences Meeting and Exhibit, Reno, NV, USA, 6–9 January 2003.
19. Nayyar, P.; Barakos, G.N.; Badcock, K.J. Prediction of flow dynamics over cavities by detached eddy simulation. *Aeronaut. J.* **2007**, *111*, 153–164. [CrossRef]
20. Rokita, T. Experimental and Numerical Investigation of the Subsonic Flow Field inside and near a Weapons Bay. Ph.D. Thesis, Technion—Institute of Technology, Haifa, Israel, 2014.
21. Kim, D.H.; Choi, J.H.; Kwon, O.J. Detached eddy simulation of weapons bay flows and store separation. *Comput. Fluids* **2015**, *121*, 1–10. [CrossRef]
22. Bacci, D.; Saddington, A.J.; Bray, D. Wavelet analysis of complex-geometry transonic cavity flows. In Proceedings of the AIAA Aviation Forum, Washington, DC, USA, 13–17 June 2016.
23. Babu, S.; Loupy, G.; Dehaeze, F.; Barakos, G.; Taylor, N. Aeroelastic simulations of stores in weapon bays using detached-eddy simulation. *J. Fluids Struct.* **2016**, *66*, 207–228. [CrossRef]
24. Sheta, E.F.; Harris, R.E.; George, B.; Ukeiley, L.; Luke, E. Loads and acoustics prediction on deployed weapons bay doors. *J. Vib. Acoust.* **2017**, *139*, 031007. [CrossRef]
25. Yalcin, O.; Ozyoruk, Y. Delayed detached-eddy simulations of transonic cavity noise. In Proceedings of the AIAA Aviation Forum, Virtual Event, 2–6 August 2021.
26. Spalart, P.R.; Jou, W.H.; Strelets, M.; Allmaras, S. Comments on the feasibility of LES for wings, and on a hybrid RANS/LES approach. In Proceedings of the 1st AFOSR International Conference on DNS/LES, Columbus, OH, USA, 4–8 August 1997.
27. Spalart, P.R.; Allmaras, S.R. A one-equation turbulence model for aerodynamic flows. In Proceedings of the 30th Aerospace Sciences Meeting and Exhibit, Reno, NV, USA, 6–9 January 1992; Volume 94.
28. Kok, J.; Dol, H.; Oskam, B.; van der Ven, H. Extra-large eddy simulation of massively separated flows. In Proceedings of the 42nd AIAA Aerospace Sciences Meeting and Exhibit, Reno, NV, USA, 5–8 January 2004.
29. Kok, J. Resolving the dependence on free-stream values for the k-ω turbulence model. *AIAA J.* **2000**, *38*, 1292–1295. [CrossRef]
30. Rossiter, J.; Kurn, A. *Wind Tunnel Measurements of the Unsteady Pressures in and behind a Bomb Bay (T.S.R.2)*; TR AERO.2677; Royal Aircraft Establishment: Farnborough, UK, 1963.
31. Shaw, L.; Clark, R.; Talmadge, D. F-111 generic weapons bay acoustic environment. *J. Aircr.* **1988**, *25*, 147–153. [CrossRef]
32. Rokita, T.; Elimelech, Y.; Arieli, R.; Levy, Y.; Greenberg, J.B. Experimental characterization of turbulent subsonic transitional-open cavity flow. *Exp. Fluids* **2016**, *57*, 60. [CrossRef]
33. Crook, S.D.; Lau, T.C.W.; Kelso, R.M. Three-dimensional flow within shallow narrow cavities. *J. Fluid Mech.* **2013**, *735*, 587–612. [CrossRef]
34. Crafton, J.; Stanfield, S.; Rogoshchenkov, N.; Palluconi, S.; Schmit, R. Measurement of unsteady forces on a store in a cavity using dynamic pressure-sensitive paint. In Proceedings of the AIAA Aviation Forum, Atlanta, GA, USA, 25–29 June 2018.
35. DeMauro, E.P.; Beresh, S.J.; Casper, K.M.; Wagner, J.L.; Henfling, J.F.; Spillers, R.W. Volumetric velocimetry of complex geometry effects on transonic flow over cavities. *AIAA J.* **2019**, *57*, 1941–1954. [CrossRef]
36. Roughen, K.; Wang, X.; Bendiksen, O.; Baker, M. A system for simulation of store separation including unsteady effects. In Proceedings of the 47th AIAA Aerospace Sciences Meeting, Orlando, FL, USA, 5–8 January 2009.
37. Barone, M.; Arunajatesan, S. Pressure loadings in a rectangular cavity with and without a captive store. *J. Aircr.* **2016**, *53*, 982–991. [CrossRef]
38. Yan, P.P.; Zhang, Q.F.; Li, J. Numerical study of strong interplay between cavity and store during launching. *J. Mech.* **2018**, *34*, 103–112. [CrossRef]
39. Levy, Y.; Raveh, D. *The EZNSS CFD Code—Theoretical and User's Manual*; ISCFDC Report 2015-06, Rev 330; Israeli CFD Center Ltd.: Caesarea, Israel, 2015.
40. Benek, J.; Steger, J.; Dougherty, F.; Buning, P. *Chimera: A Grid-Embedding Technique*; AEDC–TR–85–64; United States Air Force: Washington, DC, USA, 1986.
41. Levy, Y.; Adar, M. A multi-level parallelism approach for a chimera based implicit flow solver. In Proceedings of the 46th Israel Annual Conference of Aerospace Sciences, Tel-Aviv and Haifa, Israel, 1–2 March 2006.
42. Abe, K. A hybrid LES/RANS approach using an anisotropy-resolving algebraic turbulence model. *Int. J. Heat Fluid Flow* **2005**, *26*, 204–222. [CrossRef]
43. Batten, P.; Leschziner, M.; Goldberg, U. Average-state jacobians and implicit methods for compressible viscous and turbulent flows. *J. Comput. Phys.* **1997**, *137*, 38–78. [CrossRef]
44. Ahuja, K.K.; Mendoza, J. *Effects of Cavity Dimensions, Boundary-Layer and Temperature on Cavity Noise with Emphasis on Benchmark Data to Validate Computational Aeroacoustic Codes*; NASA CR–4653; NASA: Washington, DC, USA, 1995.
45. Schlichting, H.; Gersten, K. *Boundary Layer Theory*, 9th ed.; Springer: Berlin/Heidelberg, Germany, 2017.
46. Knowles, K.; Ritchie, S.; Lawson, N. *An Experimental and Computational Investigation of a 3D, l/h = 5 Transonic Cavity Flow*; Technical report; U.S. Air Force Academy: Colorado Springs, CO, USA, 2007.